AN ABSTRACT OF THE THESIS OF

Jonah M. Gross for the degree of Master of Science in

Electrical and Computer Engineering presented on March 7, 2013.

Title:

Development of Acoustic Transducers for Use in the Parametric Pumping of Spin Waves

Abstract approved: ____

Pallavi Dhagat

The work detailed here is the development of simulations and fabrication techniques used for the construction of thin-film acoustic transducers for use in the parametric pumping of spin waves. The Mason Model, a 1-D equivalent circuit simulating the responses of multilayer acoustic transducers, is implemented using ABCD-parameters in MATLAB to determine the expected response from fabricated devices. The simulation is tested by varying device parameters and comparing the changes in device resonance response to those of prior published results. Three-layer thin-film acoustic transducers were also fabricated. These transducers use zinc oxide (ZnO) as a piezoelectric layer with aluminum (Al) electrodes. Construction is accomplished using the common thin-film fabrication techniques of sputtering, thermal evaporation, etching, and lift-off patterning processes. The response of the fabricated transducers is compared to that of the simulated response by observing the transducer's resonance frequency and characteristics. These results are used to validate the simulation and the transducer fabrication process. Finally, their usefulness for the design and fabrication of an acoustic spin wave amplification system is considered.

©Copyright by Jonah M. Gross

March 7, 2013

All Rights Reserved

Development of Acoustic Transducers for Use in the Parametric Pumping of Spin Waves

by

Jonah M. Gross

A THESIS

submitted to

Oregon State University

in partial fulfillment of
the requirements for the
degree of

Master of Science

Presented March 7, 2013
Commencement June 2013

Master of Science thesis of Jonah M. Gross presented on March 7, 2013.

APPROVED:

Major Professor, representing Electrical and Computer Engineering

---

Director of the School of Electrical Engineering and Computer Science

---

Dean of the Graduate School

I understand that my thesis will become part of the permanent collection of Oregon State University libraries. My signature below authorizes release of my thesis to any reader upon request.

Jonah M. Gross, Author

ACKNOWLEDGMENTS

Most of all, I would like to thank my loving wife, Alice, who has supported me through this long and difficult process and never let me give up. My entire family also deserves much thanks; without your love and support I could not have reached this point.

I would also like to extend an acknowledgment to my advisor, Dr. Dhagat, and a special thanks to a mentor of mine, Dr. Plant, whose contribution to my education, and countless others at OSU, has been invaluable.

TABLE OF CONTENTS

TABLE OF CONTENTS (Continued)

LIST OF FIGURES

LIST OF FIGURES (Continued)

LIST OF TABLES

DEVELOPMENT OF ACOUSTIC TRANSDUCERS FOR USE IN THE PARAMETRIC PUMPING OF SPIN WAVES

1. INTRODUCTION

Acoustic oscillators have been in use in the field of electronics for decades, with applications ranging from oscillators for time keeping, to sensors measuring flow rates or detecting trace gases. This thesis presents the development of thin-film acoustic transducers for use in creating an acoustic spin wave amplification system. The eventual goal of this work is to parametrically pump propagating spin waves in a magnetic oxide film (Yttrium Iron Garnet); however, the main focus and motivation of this work is the simulation and fabrication of the transducers needed to accomplish this goal.

Spin waves have been an area of interest for many years, traditionally as a loss mechanism in magnetic systems or as a purely scientific study into their properties. Recently, however, there has been renewed interest, as they have become a candidate to be a signal carrying medium and even conduct logic operations [1, 2]. A primary reason for this interest is the nature of the spin waves. Spin waves are a pure spin current, meaning the signal is not only carried by the spin of the electron rather than its charge, but the electrons do not move through the material, resulting in no heat creation. A major draw back, that the acoustic spin wave pump looks to address, is the high attenuation of spin waves in most materials. The spin wave pump will act as a repeater in a spin-wave-based transmission system, allowing signals to propagate over longer distances and to be used in more operations.

In this work, a simulation implementing the Mason Model [3, 4] is created using MATLAB to predict the response of acoustic transducers to help in the design process. The simulation takes into account the multiple layers in the acoustic transducers that affect the response, namely acoustic loading due to electrode layers and physical properties, such as layer thicknesses and material properties. Transducers are also fabricated and measured, comparing their response to that predicted by the simulated model.

This thesis is divided into six chapters, this being chapter one and providing an introduction to the project including motivation and project goals. Chapter two presents background information necessary for the work featured. This includes piezoelectric acoustic transducers, the physics behind resonators, which is useful in understanding transducer operation, and a discussion of material properties pertinent to acoustic transducers, namely the piezoelectric properties of zinc oxide (ZnO). Chapter three discusses the fabrication processes used in making acoustic transducers in the laboratory, including deposition and patterning techniques. Chapter four details the simulation created to model transducer response to assist in the analysis of the fabricated transducers, as well as measurement techniques used to measure their response. Chapter five shows the results observed from experiments conducted on the simulation and the measurements taken from the fabricated transducers. Finally, chapter six gives a summary of the results and conclusions drawn from the experiments conducted as well as suggested next steps in the project of creating an acoustic spin wave pump.

DEVELOPMENT OF ACOUSTIC TRANSDUCERS FOR USE IN THE PARAMETRIC PUMPING OF SPIN WAVES

2. LITERATURE REVIEW

We begin with some necessary background information that will assist with the understanding and modeling of thin-film acoustic transducers. Presented here is an overview of acoustic transducers with details including topology and structure as well as the concepts of resonance and piezoelectricity. Focus is also given to material properties, namely those important to piezoelectric materials and their effect on transducer device operation.

2.1 Acoustic Transducers

Acoustic transducers are devices that transform electrical energy to and from acoustic energy. The most commonly thought of application is in audio applications, where microphones and speakers transform audio signals to and from electrical signals. In this work however, the frequency range is much higher, approximately 1 GHz - 8 GHz. This frequency range is used as it is where the ranges of acoustic transucers and spin wave excitation/detection experiments overlap. To achive the desired parametric pumping of spin waves, the acosutic frequency must be twice the spin wave frequency. High frequency acoustic transducers are used in a wide variety of applications across many disciplines, including, but not limited to: reference frequency generation, biomolecule detection [5], ultrasonic imaging, signal processing and gas flow metering [6]. All piezoelectric transducers can be separated into two main categories based on the wave propagation mode, Bulk Acoustic Waves (BAW) and Surface Acoustic Waves (SAW) (Fig. 2.1). BAWs propagate through the interior of a material as either longitudinal (compression) or transverse (shear) waves, while SAWs propagate on the surface and are usually dominated by

Rayleigh waves, which are a combination of both longitudinal and transverse waves that are localized to a surface. The transducers implemented in this work are thin-film bulk acoustic resonators (TFBAR) and fall into the longitudinal BAW category. Compression waves are propagated through the excitation of a ZnO layer down into the substrate.

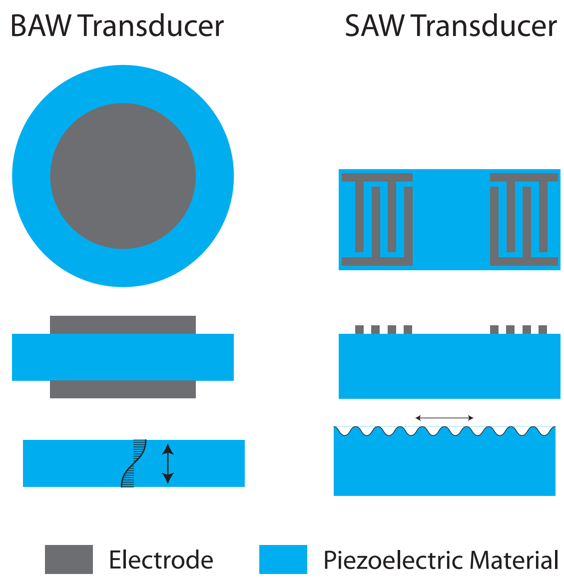

Figure 2.1: BAW and SAW transducers showing wave propagation direction in each device.

2.1.1 Resonance

Some acoustic transducers, such as TFBARs, take advantage of a property called resonance. An oscillator exhibits resonance when, at certain frequencies, small changes in the oscillatory system results in higher changes in the oscillation amplitude. These frequencies, called resonant frequencies, occur when feedback within the oscillator constructively interacts with the oscillation. This frequency is a function of the physical properties of the oscillator. For example, in a simple pendulum, it depends mostly on the length of the swinging arm. For TFBARs, a primary factor is the piezoelectric film thickness and is important for the design of transducers and determining their frequency operating point.

2.1.1.1 Resonators

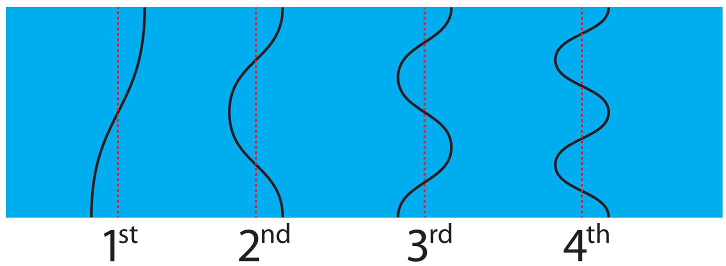

Figure 2.2: A resonant cavity with the first four resonances shown.

For TFBARs, a resonance occurs when the acoustic waves propagating in the piezoelectric layer are reflected back from the interface with the next layer and constructively interfere with the original propagating waves. This condition occurs when the piezoelectric layer thickness is an integer multiple of $1/2$ the wavelength of the acoustic wave (Fig. 2.2). Equation 2.1 describes the resonant frequency of a cavity terminated on both ends by the same termination (both open or both short) where n is an integer (1,2,3...), v is the velocity of the propagating wave, and t is the length of the cavity.

$$f = \frac{nv}{2t} \tag{2.1}$$

2.1.1.2 Q-Factor

The Q-factor, often referred to simply as the Q, is a unitless value commonly used to describe resonator responses. The Q of a resonator has several physical meanings and implications. By definition it is a measure of how much energy is lost during oscillation (Eq. 2.2), or how much energy it takes to keep the oscillation going. This means that the damping of a oscillating system plays a major role in determining the Q. In the frequency domain, the Q is defined by the resonance frequency over the width of the resonant peak (Eq. 2.3) at half power. Higher Q systems not only have lower losses, but also tend to see larger responses to stimulus. That stimulus however, must fall within a smaller frequency envelope, making selectivity of the operating more important as the response falls off more rapidly away from the resonance frequency. In this work, Q-factor is used as a qualitative tool to analyze effects resonator parameters have on operation.

$$Q \approx \frac{\text{Energy stored}}{\text{Energy lost per cycle}} \tag{2.2}$$

$$Q = \frac{f_r}{\Delta f} \tag{2.3}$$

2.1.2 Material Properties for Thin Film Bulk Acoustic Resonators

In TFBARs, the material of highest interest is the piezoelectric layer. It is the piezoelectric effect that allows for the oscillations that cause the acoustic waves. The piezoelectric effect is caused when an asymmetrical crystal undergoes stress causing a shift in charge distribution within the crystal lattice, resulting in the generation of an electric field. This field is due to the unbalanced charge distribution within the crystal lattice creating a local dipole. These dipoles, when added up over the volume of the piezoelectric material, cause the buildup of charge on the surface of the material. The inverse-piezoelectric effect also occurs. When an electric field is applied to the piezoelectric material, dipoles are generated to counter the applied field, resulting in a deformation of the crystal. The piezoelectric material of choice for this work is ZnO. Chosen for its ease of use, ZnO's most stable form exhibits a Wurtzite crystal structure, which lacks a crystal inversion center, giving it piezoelectric properties. When designing acoustic transducers, several properties of the piezoelectric material are important. ZnO, like many piezoelectric material, exhibits anisotropy in its acoustic and piezoelectric properties. The primary piezoelectric axis for ZnO is in the z-direction, requiring material properties that match. For ZnO, this corresponds to the $_{33}$ crystal direction. The piezoelectric stress constant (e_{33}) relates the stress on the material to the electric field generated and is the primary piezoelectric constant. Other material properties important to transducer operation are the elastic stiffness constant (c_{33}) and the material density (ρ). Together, these properties determine the velocity of acoustic waves propagating through the material and govern the acoustic properties. The subscripts on the piezoelectric and elastic stiffness constants denote directionality since these properties are anisotropic. For ZnO these constants are: $e_{33} = 1.34$ Cm^{-2}, $c_{33} = 211$ GPa, and $\rho_{ZnO} = 5606$ kgm^{-3} [7, 8]. These properties will play a major role in the simulation that will be discussed in the coming chapters.

3. FABRICATION

The fabrication of the acoustic transducer devices was accomplished using several physical vapor deposition (PVD) methods for the creation of thin-films in conjunction with several patterning techniques. The methods used depend both on the material being deposited as well as the desired thin-film properties, including size, shape, uniformity, and crystal orientation. The techniques and methods used in this research are discussed in the following section.

3.1 Thin-Film Deposition Methods

During the fabrication process, two thin-film deposition methods were used, thermal evaporation and magnetron sputtering. The physics of both methods, as well as their practical implications are discussed and detailed below.

3.1.1 Thermal Evaporation

Thermal evaporation is used to deposit metals. In the research presented, it is used to deposit aluminum thin-films. A small sample of the material is heated beyond its melting temperature in a vacuum chamber (pressure $< 1x10^{-5}$ Torr) where it has enough kinetic energy to evaporate and recondense on the substrate material suspended above the source (Fig. 3.1). To accomplish the heating, the source material is placed in a basket shaped filament mounted between two electrodes. A high current (10's of amps) is passed though the filament causing the entire fixture to heat up due to resistive heating which melts the metal. The filament material must be chosen such that the melting temperature

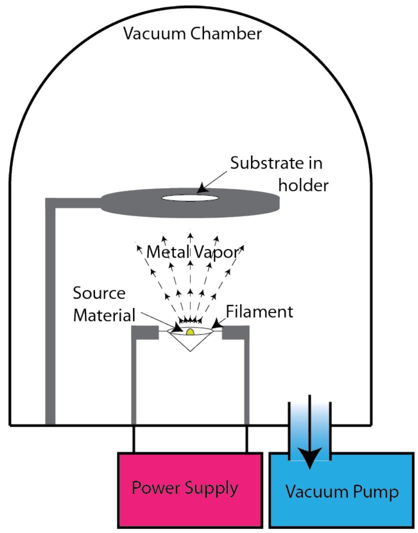

Figure 3.1: A schematic view of a thermal evaporation deposition tool.

is much higher than that of the material to be deposited in order to ensure no disruption in current flow due to loss of contact. A common filament material used is tungsten as it has a high melting temperature of 3422 °C, as compared to aluminum with a melting temperature of 666 °C.

This evaporating metal acts as a point source within the deposition chamber, meaning that every surface with line of sight to the filament is coated with metal. This has several implications. The first, and simplest, is that this process cannot be observed directly, any window that is used to view the filament to observe when the material is melted will be coated with evaporated material, i.e., Al, and become opaque. This means that another method must be used to determine when the metal has melted and begun to evaporate. There are two methods commonly used to accomplish this, the first and simplest way is to observe the chamber pressure and watch for a sudden increase which signifies the vaporization of the metal. This increase is due to the introduction of new particles to the vacuum environment, the evaporated metal. Thickness can be controlled through characterization of the deposition rate through experimentation and varying the exposure time to get the desired thickness. Another, more elegant (and useful) method uses a quartz crystal oscillator. For a crystal oscillator, the fact that all surfaces facing the source are coated is exploited. The oscillator is placed in the chamber exposed to evaporation source. As the surface of the oscillator is coated, the build up of material causes a change in the oscillation frequency based on the amount of metal deposited on the oscillator. When placed at the same distance from the source as the substrate, the crystal oscillator makes it possible to accurately establish both the deposition rate and the total deposited thickness.

The second, and more serious, implication of the point source deposition dynamic has to do with film uniformity and coverage. Since the material flux density is inversely related to the square of the distance from the source, the thickness of the deposited material will vary over the substrate surface (Fig. 3.2). This variation can be avoided if the substrates are mounted on a curved fixture, such that they are all a uniform distance from the filament. The substrates used here are mounted in a flat fixture, so the thickness of the deposited material are not uniform over the entire substrate area. When thickness and uniformity are important, as they are in most microelectronic fabrication cases, this non-uniformity can be catastrophic. The non-ideal deposition angle in point source deposition did however lead to an unintended benefit; when the substrates are oriented correctly in the deposition chamber, better electrical connectivity over large steps in underlying layers is found. This was due to metal deposition on the side of the step face resulting from the off axis angle to the point source.

3.1.2 Magnetron Sputtering

Magnetron sputtering deposition involves accelerating ions into a solid comprised of the material, called a target, that is to be deposited. The ions transfer their momentum into the target material, causing several atoms to break loose from the surface. These atoms are then able to re-condense on surfaces in the deposition chamber.

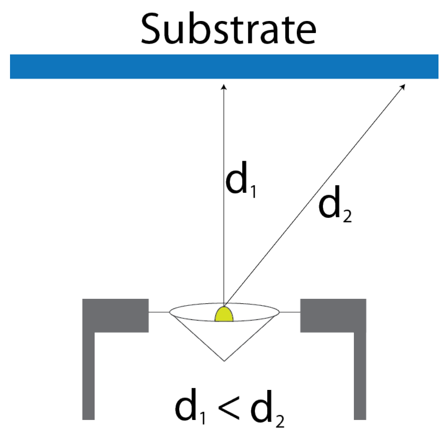

Figure 3.2: Deposition from a point source onto a flat substrate results in a thickness gradient in the deposited film due to the variation in distance to the source over the entire substrate.

To create this ion bombardment, a plasma is created just above the surface of the target through the application of a high electric field to a low pressure gas, usually a non-reactive gas such as argon or neon. Any electrons entering the field are accelerated to a point where when they impact a gas atom, they cause ionization through removal of an outer shell electron. This newly freed electron, along with the original electron, are free to accelerate again to impact another gas atom, resulting in a chain reaction. The plasma is maintained and contained through the application of a toroidal magnetic field just above the target surface. This magnetic field alters the path of the free electrons in the plasma such that they spiral around rather then traveling in a straight line. This longer path greatly increases the likelihood of a collision with a gas atom, causing another ionization. These newly created ions are also accelerated by the electric field and smash into the target, transferring their momentum to the surface atoms. It is this momentum transfer that dislodges atom from the target for deposition.

On the surface of the target, if the target is conductive, electrons will immediately move to counter the positive charge from the introduced ion. In an insulating target however, like ZnO, the introduced positive charge is not countered by the targets internal electron gas, resulting in a buildup of positive charge on the target surface. This buildup will reduce the effective field between the electrode and the target used to accelerate the ions into the surface, reducing number of electrons that have enough energy to break loose target atoms, effectively reducing the sputter rate. To counter this buildup, the target is biased with an alternating rf voltage. The RF bias accelerates ions into the surface for sputtering during the negative portion of the cycle, and expels the built up positive charge on the surface during the positive portion.

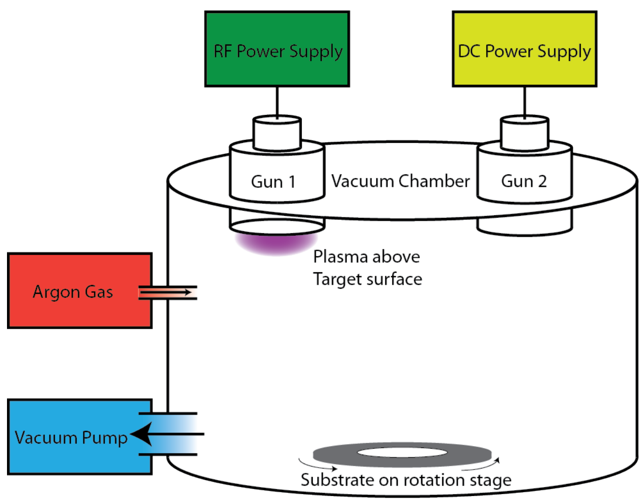

Figure 3.3: A schematic view of an off-axis, sputter-down deposition chamber. The RF supply is used for insulating targets and the DC supply for conductive targets. The substrate is placed on the rotating stage to maximize film uniformity.

Controllable process parameters for RF magnetron sputtering include: gas flow rate and species, power applied to target, substrate positioning and motion, and deposition time. Changes in gas flow rate are used to set the chamber operating pressure. This pressure must be balanced to provide enough gas atoms for a high target bombardment rate while keeping collision of sputtered atoms with neutral gas atoms in the chamber to a minimum, maintaining a long mean free path. If the mean free path is too short, the sputtered atoms from the target will collide with gas atoms before they reach the substrate, altering their path and reducing their energy, thus making it less likely they will reach the substrate. The use of the magnetic field above the surface of the target greatly increases the probability of a gas atom becoming ionized and accelerating into the target, effectively reducing the pressure needed to maintain a plasma above the target. This allows for a lower operating pressure, which in turn increases the mean free path of the sputtered atoms, yielding higher deposition rates. A reactive gas can also be introduced to the chamber to alter the composition of the deposited film. The sputtered atoms react with the ambient gas during flight creating a different, desired material, for example, introducing O_2 to a sputter chamber with a Zn target to deposit ZnO. This process is known as reactive sputtering. For this research, O_2 is introduced into the sputter chamber with a ZnO target to reduce the disassociation of the Zn and O atoms during the sputter process and maintain desired film stoichiometry.

Target power is the amount of power applied into the plasma and is directly related to the sputter rate. It is a measure of the plasma current flowing due to charged particles moving through the plasma to bombard the target surface. A higher target power creates higher bombardment rate, resulting in a higher sputter rate. Practical limitations to target power come from the supply equipment being used, but also the heat dissipation ability of the gun and target. Ceramic targets tend to have higher thermal resistances, limiting the amount of power that can be applied before thermal damage occurs. Care must also be taken in making changes to the applied power as thermally induced stresses can result in target cracking and cause permanent damage to the target.

Physical control of the sputter chamber also allows for control over film deposition properties. The most basic control involves the motion and placement of the substrate.

Depending on chamber geometry, the substrate can be placed on or off axis with the sputter gun (Fig. 3.4). This placement affects several deposition parameters, primarily

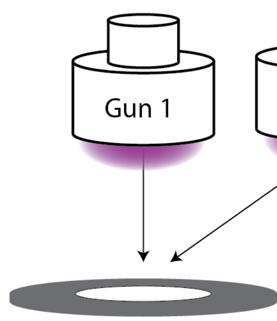

Figure 3.4: Gun 1 is positioned on-axis with the substrate and will yield a higher deposition rate. Gun 2 is off-axis and, when paired with a rotating substrate, will result in a film with greater uniformity.

deposition rate and film uniformity. The distance from target to substrate also affects deposition parameters. Optimal operating distance is important for several reasons, a balance between deposition rate and film quality must be reached. Too close, and the particle flux can cause secondary sputtering on the substrate, damaging both the newly deposited film, and the substrate itself. Too far, and the rate will fall to an impractically low level. Increasing the distance also increases the film uniformity over the entire substrate, which can be further augmented through rotation of the substrate relative to the target. In the sputter tool used in this work, all guns have an off-axis positioning and sample distance of approximatively 10 cm.

3.2 Patterning

With deposition techniques established, the deposited films must be patterned into functional shapes. This is accomplished through the use of photolithography. Patterning techniques, including etching and lift-off, are described in the following section.

3.2.1 Photolithography

Photolithography is a backbone of modern micro-fabrication technology. It allows for the transfer of precises patterns into fabrication materials through the selective application of light. A thin layer of photoreactive material, called photoresist (PR), is deposited on the surface of the substrate. When exposed to select wavelengths of light, the bond strength within the photoresist is altered. There are two main types of photoresist, positive and negative, referring to the type of alteration to the bond strength, weakening or strengthening respectively. Once exposed, the photoresist is submerged in a solvent that breaks down the photoresist with weaker bonds, leaving only the strongly bonded regions (unexposed for positive and exposed for negative) on the surface of the substrate as shown in Fig. 3.5. It is this remaining photoresist that is used to transfer the pattern to the desired material.

3.2.1.1 Etching

The most commonly used patterning method is etching. The basis of this technique is to use the patterned photoresist as a protective layer for the material underneath, meaning only areas not covered by photoresist will be affected by the etching process. A diagram showing this process can be seen in Fig. 3.6.

Etching comes in two primary flavors, often referred to as wet and dry, describes the manner in which material is removed from the surface. The first method, wet etching, involves submerging the sample in an aqueous solution of a reactive chemical, often an

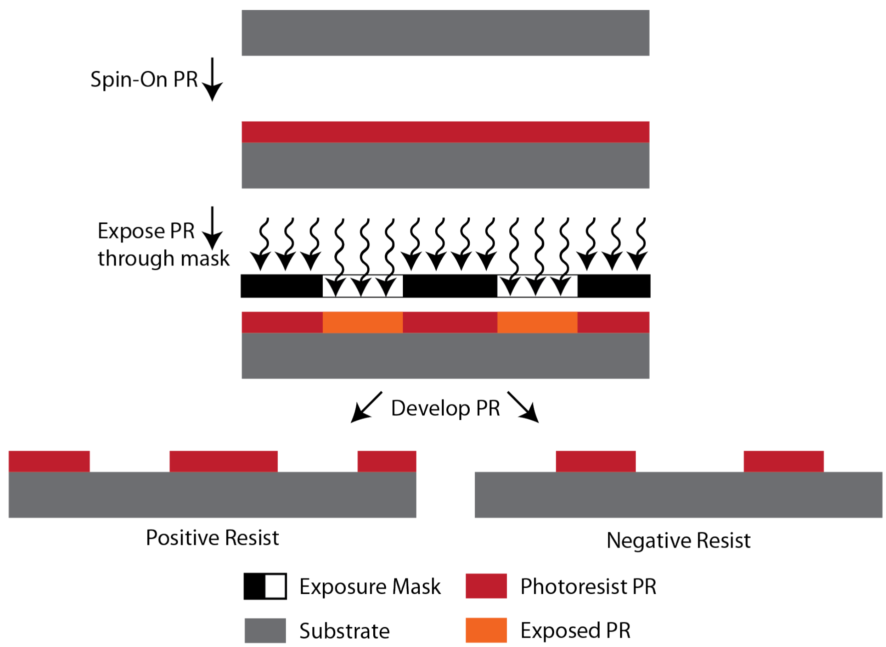

Figure 3.5: A process using the two types of photoresist, negative and positive, is shown demonstrating the opposite pattern generated with each.

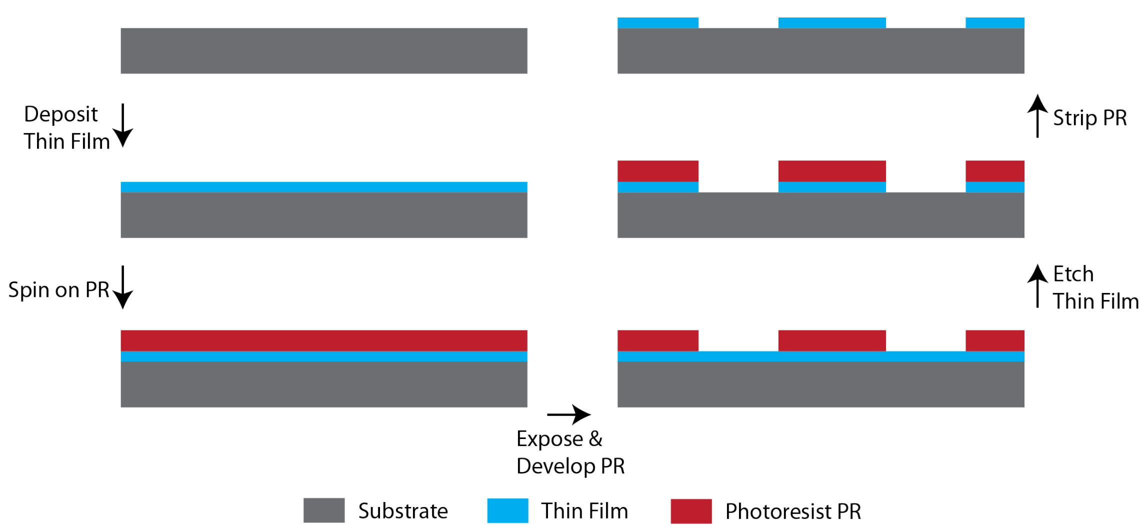

Figure 3.6: A sample process flow showing how a pattern is transfered to a thin film using an etching technique. Photoresist is deposited and patterned on top of the target thin film. It is then exposed to an environment that removes the exposed material.

acid, that will react with and dissolve the material to be etched. Careful selection of this etchant gives wet etching one of its major advantages; if the etchant reacts with only the material to be etched, layers can be completely removed without damaging underlying layers. Wet etching has a major disadvantage however, because the sample is submerged in a fluid, the newly exposed sidewalls of the etched area are also exposed to the etchant, resulting in an isotropic etch (Fig. 3.7). When etching a crystalline material however, the

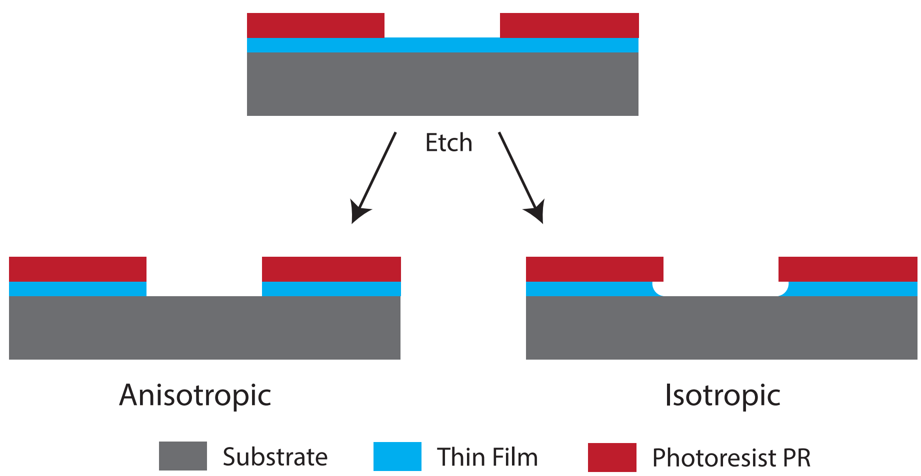

Figure 3.7: The two extremes for etch profiles, isotropic and anisotropic. Wet etches will often have an isotropic profile because the etchant reacts with the side walls of the hole being etched, resulting a some horizontal direction of the etch. This process, where the material is etched out from under the photoresist is known as under cutting.

etch may become slightly anisotropic as different crystal faces will etch at different rates. This allows for the use of substrate crystal orientation to determine feature profile, as well as the design of etchants that maximize the etch anisotropy. The isotropic nature of wet etches allows the etchant to undercut the photoresist mask used to protect the desired pattern. Undercutting of the photoresist results in features that are larger then intended. Practically, this limits the minimum feature size of patterns to be etched with a wet etch process and makes it most useful for removing material from large area.

The other etching process, commonly referred to as dry etching, was not used for this project so will only be mentioned briefly and with limited detail for completeness of the discussion. For more information see *Silicon Processing for the VLSI Era* by Wolf and Tauber [9]. Dry etching uses ions to chemically or mechanically remove atoms from the sample surface and has the major advantage of being capable of highly anisotropic etching. Dry etching techniques tend to have less selectivity than wet etching, increaseing the likelihood of causing damage to underlying layers. Careful design and application of dry etching techniques can minimize these effects making it a very valuable and vital patterning process.

3.2.1.2 Lift-off

Lift-off is essentially the opposite of an etching process. In a lift-off process, the photoresist is deposited directly on the substrate before the thin-film material to be patterned is deposited. This means that when the thin-film is deposited, some of it will be on top of the photoresist and only areas lacking photoresist will have material on the substrate. When the photoresist is removed, only material on the substrate will remain, leaving the desired pattern (Fig. 3.8).

One of the major advantages to lift-off is the reduction of damage to underlying layers that can be caused by other etching methods. The only material that needs to be removed is the photoresist which is designed to be easily removed. There is no need to develop selective etchants that only remove desired materials and no risk of etching too deep and removing substrate or underlying material. There are however downsides; in order for the lift-off process to work, the film being deposited must be thinner than the photoresist layer, allowing for breakdown of the photoresist under the deposited film. Another major concern when using lift-off is tearing of the thin-film. With the photoresist removed, the thin-film on top is free to float away. If the tin film is still attached at a point,

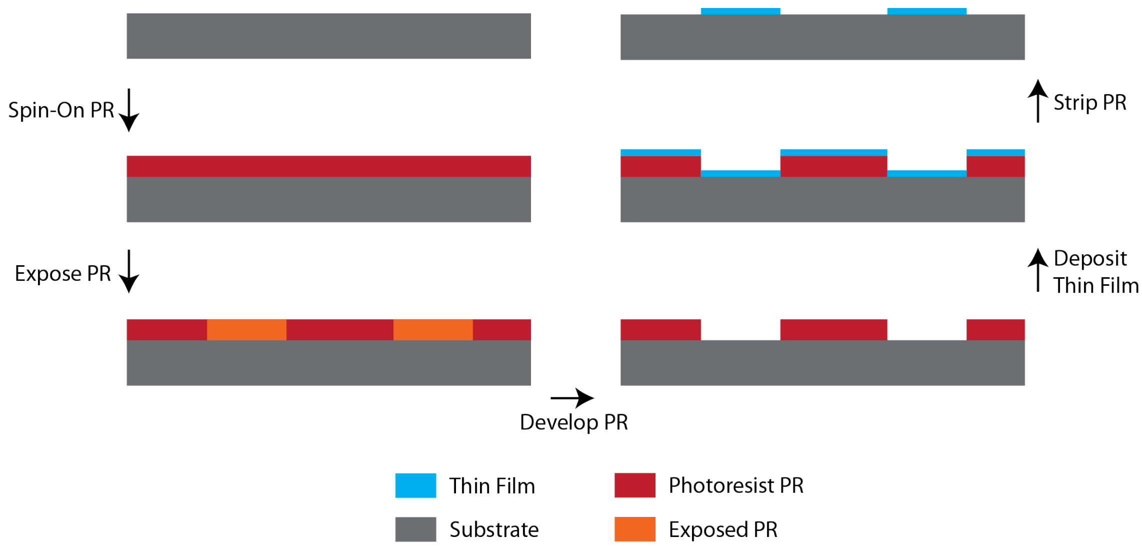

Figure 3.8: A lift-off process flow is shown to demonstrate the patterning technique. The thin film is deposited on top of the patterned photoresist resulting in only material deposited directly to the substrate remaining after stripping of the photoresist. Note the pattern generated is opposite that of an etching process.

such as a corner, it can tear some of the material on the surface off with it, causing defects in the desired pattern. This problem can be exacerbated when the application of sonic frequency vibrations (sonication) is used to agitate the sample and assist in the removal of the photoresist. Maximizing film-substrate adhesion as well as control of sonication power can greatly reduce the occurrence of tears in the patterned thin-film. Luckily, the large feature sizes of the devices in this work are not as susceptible to tearing as smaller more delicate features. Still, sonication power is kept at a low level during fabrication to ensure minimal risk.

3.3 Fabrication Process Flow

For the fabrication of the acoustic transducers, the deposition and patterning methods were combined into a complete process, as shown in Fig. 3.9. The fabricated devices consist of a stack of Aluminum(100 nm-200 nm)/Zinc Oxide(600 nm-1200 nm)/Aluminum(100 nm-200 nm). All layer thickness are determined through the use of a step profilometer, where a needle tip is dragged across the surface of the device, measuring changes in the surface hight. Initially, the aluminum layers were deposited using thermal evaporation due to its ease and on site access in the OSU cleanroom. Deposition was done in a Poloron desktop thermal evaporation tool with a chamber pressure of less then 3.5 x 10^{-5} mTorr, a maximum boat current of 20 A and a coat time up to 30 sec. For later devices however, a sputtered Al layer is used because of its higher uniformity and thickness control offered by the tool used. This higher level of control was necessary due to the sensitivity of the acoustic properties of the device to the layer thicknesses. The ZnO was deposited using a sputter process as well, with an addition of oxygen to the normal argon chamber gas to keep the oxygen levels within the film from being depleted during the deposition process. Both materials were deposited using an AJA sputter system with a chamber pressure of 3.4 mTorr. The ZnO deposition is done in an RF gun with a gas flow rate of 18 sccm Ar and 2 sccm O_2, maintaining the manufacturer recommended 20 sccm total flow rate, and a target power of 150 W. The substrate is also heated to $200°C$ and held their for the duration of the ZnO deposition. The Al deposition is done with a DC gun with a gas flow rate of 20 sccm Ar and a target power of 200 W. The deposition time is varied to control film thickness, with a ZnO deposition rate of 1.3 nm per minute and a Al rate of 20 nm per minute. Patterning was done in three mask steps, bottom electrode, ZnO layer, and top electrode (Fig. 3.10a). Both Al electrode layers were patterned using a lift-off process and the ZnO using a 200:1 H_2O:HCl etch. A summary of the processing parameters used can be found in table 3.1 and a photograph of a transducer fabricated on glass in Fig. 3.10b.

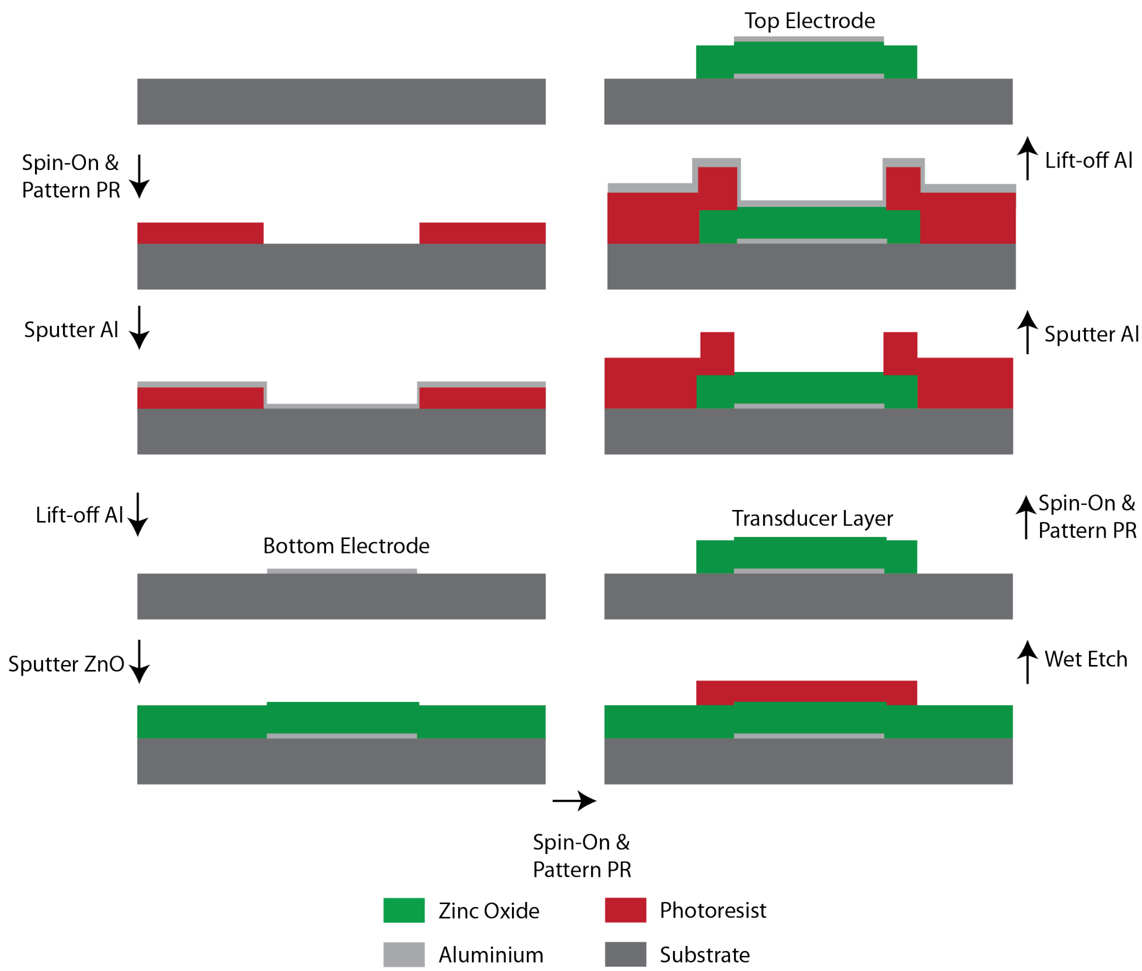

Figure 3.9: A schematic process flow showing the steps taken to create thin-film acoustic transducers.

Deposition				
Process	Pressure	Gas Flow Rate	Power	Substrate Temp.
Al Sputter	3.4 mTorr	20 sccm Ar	200 W	N/A
ZnO Sputter	3.4 mTorr	18 sccm Ar 2 sccm O_2	150 W	$200°C$
Patterning				
Process	Solution		Agitation	
Lift-off	Acitone		Sonication	
ZnO Etch	200:1 H_2O:HCl		Light Manual	

Table 3.1: Processing parameters used for the fabrication of the acoustic transducers.

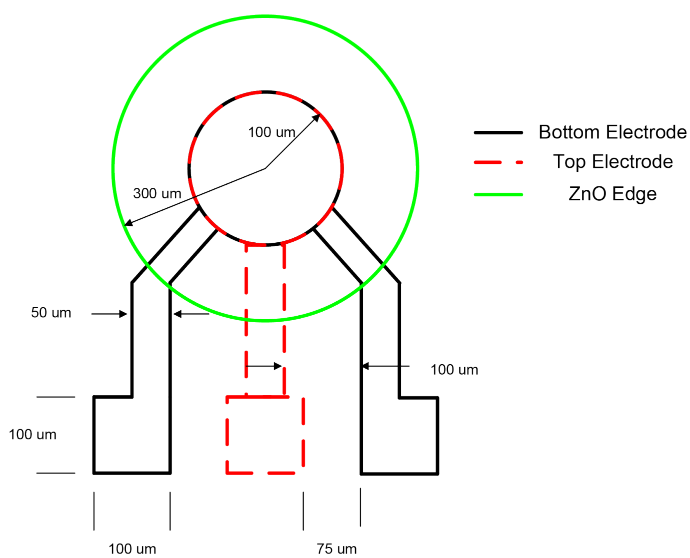

(a) Acoustic transducer fabrication mask layers with dimensions labeled.

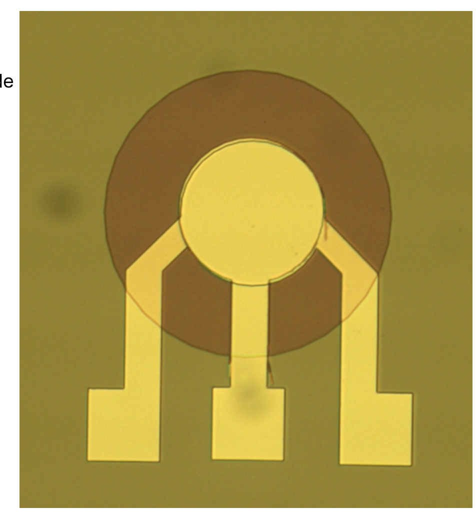

(b) Photograph of a fabricated acoustic transducer.

Figure 3.10: Acoustic Transducer

4. MEASUREMENT & ANALYSIS

With a method for fabrication of acoustic resonator established, and an understanding of the basic principles, an experimental setup can be developed to measure and analyze acoustic resonator devices. At this stage in development, the project is approached in two parts: development of a simulation to model the transducer operation, and verification and characterization of fabricated thin-film bulk acoustic transducers. This simulation is created through the application of an equivalent circuit model of the acoustic system that can be compared to the observed experimental results. The equivalent circuit model [3, 4], as well as the experimental techniques and setups used, are explained in this chapter.

4.1 Acoustic Transducer Modeling & Measurement

The second portion of the experiments conducted involves measurement and characterization of the thin-film acoustic transducers discussed in section 3.3. The goal of this line of experimentation is to verify the successful fabrication and operation of acoustic transducer devices. This is accomplished by exciting the devices and observing an acoustic resonance at the expected frequency. The expected resonance frequency is calculated based on a 1-D circuit approximation model known as the Mason model. This section will outline and discuss this model as well as measurement techniques used to analyze the fabricated devices.

4.1.1 Mason Model Equivalent Circuit

The Mason Model is a 1-D circuit model representation of an electro-acoustic system commonly used for the design of acoustic systems. Acoustic layers are represented by delay lines with piezoelectric layers having the addition of a transformer to convert electrical into acoustic energy, and vice versa. This design differs slightly from other models, such as the Krimholtz, Leedom and Matthae (KLM) model [10], where layers of acoustic material are represented as transmission lines. These two models were compared by Sherrit, et al. [11] and determined to be effectively equivalent. The Mason model is often considered flawed because it contains a negative capacitance that thought to be "unphysical." For a comuputer simulation however, component physicality has no affect on the results.

The piezoelectric layer of the circuit model (Fig. 4.1) is a three port circuit with Port 1 being in the electrical domain and Ports 2 and 3 in the acoustic domain. The electrical signal is applied to port 1 and transformed into an acoustic one via an ideal transformer. On the acoustic side of the transformer, voltage is representative of force applied and current represents particle velocity at the surface. This means that a surface terminated to air applies no force and is free to move, modeled as a short, and a mounted surface is immobile and applies a force to its substrate, modeled as an open. Anything in between uses the acoustic impedance (Z_o in Eq. 4.1) as a termination. In the acoustic domain, layers of material are modeled as T-network delay lines (Fig. 4.2) that can be connected in series to form multi layer devices. Equation 4.1 details the variables used in the equivalent circuit diagram, with t the layer thickness in meters, A the area in m^2, c_{33} the elastic stiffness constant in Nm^{-2}, v the acoustic velocity in the layer material in $\frac{m}{s}$, e_{33} the piezoelectric constant in Cm^{-2}, ρ the layer material density in $\frac{kg}{m^3}$, ε the layer permittivity, and k the acoustic wavenumber.

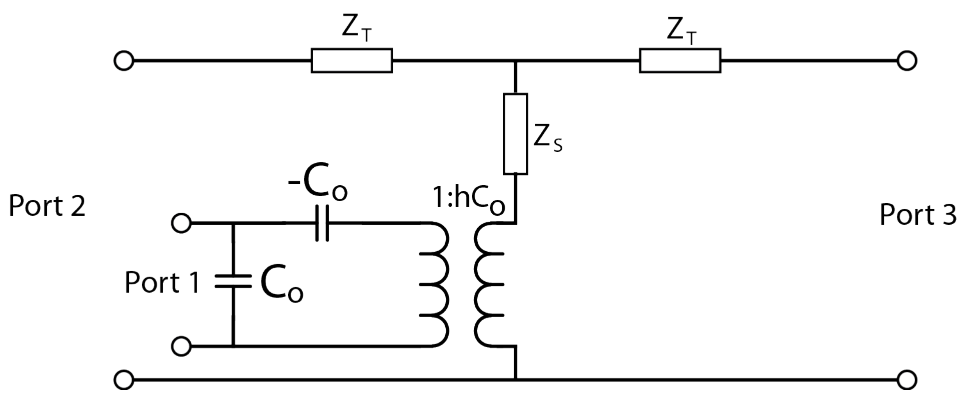

Figure 4.1: Mason model equivalent circuit of a piezoelectric layer.

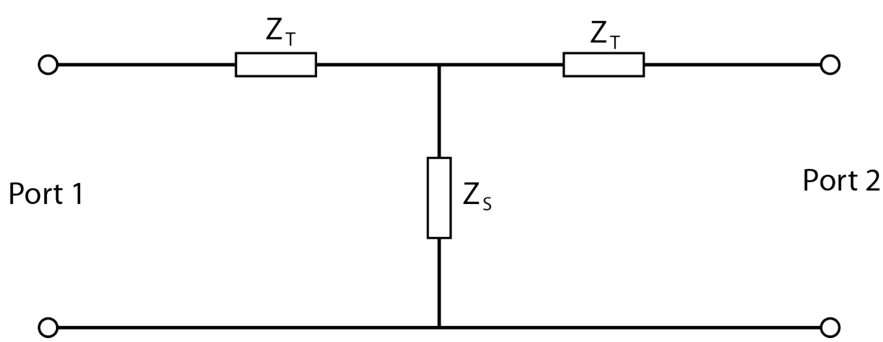

Figure 4.2: Mason model equivalent circuit of an acoustic layer.

$$
\begin{aligned}
Z_T &= jZ_o \tan\left(\frac{kt}{2}\right) & Z_S &= \frac{-jZ_o}{\sin(kt)} \\
Z_o &= \rho A v & C_o &= \frac{\varepsilon A}{t} \\
h &= K_t\sqrt{\frac{c_{33}}{\varepsilon}} & c_{33} &= \rho v^2 \\
K_t &= \sqrt{\frac{e_{33}^2}{c_{33}\varepsilon}}
\end{aligned}
\tag{4.1}
$$

For the devices fabricated, three layers are modeled, a piezoelectric ZnO layer with aluminum electrodes on either side. The substrate is represented by the termination applied to the bottom of the stack. The circuit is contrusted by attaching layer circuits to both acoustic ports of the piezoelectric layer equivalent circuit and terminating in a substrate equivalent impedance (Fig 4.3).

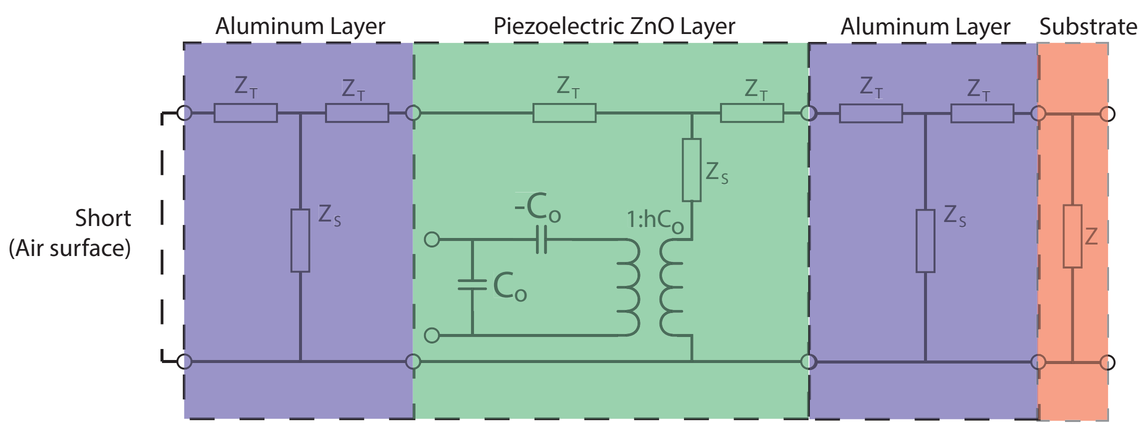

Figure 4.3: Complete Mason eqivalent circuit model for a TFBAR.

4.1.1.1 MATLAB Simulation Development

To evaluate this circuit, ABCD parameters were created that represented each layer in the stack. This method was selected due to the ability to easily connect blocks in series, as is done when connecting layers of the equivalent circuit for multi layer devices.

4.1.1.2 ABCD Parameters

ABCD parameters are used to describe the operation of a two port black box circuit element. They are particularly useful because they may be cascaded to connect several black boxes in series. To begin, the inputs and outputs are defined as the voltage and current at each port (Fig. 4.4) and the operational matrix is established (Eq. 4.2). When equation 4.2 is evaluated, the results (Eq. 4.3) are a relationship between the input and output of the black box, with the relational constants being A, B, C, and D.

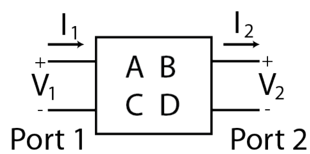

Figure 4.4: ABCD block interface definitions.

$$\begin{bmatrix} V_1 \\ I_1 \end{bmatrix} = \begin{bmatrix} A & B \\ C & D \end{bmatrix} \begin{bmatrix} V_2 \\ I_2 \end{bmatrix} \tag{4.2}$$

$$\begin{aligned} V_1 &= AV_2 + BI_2 \\ I_1 &= CV_2 + DI_2 \end{aligned} \tag{4.3}$$

To determine these relational constants, both equation are solved for the extreme cases, namely when the output is short or open. This evaluation leads to the parameter definitions in equation 4.4.

$$\begin{aligned} A = \left.\tfrac{V_1}{V_2}\right|_{I_2=0} \quad B = \left.\tfrac{V_1}{I_1}\right|_{V_2=0} \\ C = \left.\tfrac{I_2}{V_2}\right|_{I_2=0} \quad D = \left.\tfrac{I_1}{I_2}\right|_{V_2=0} \end{aligned} \tag{4.4}$$

With the basis of ABCD parameters established, they can be applied to basic circuit element blocks, building a library the more complicated circuits can be built from. The first building block is a simple series impedance (Fig. 4.5). A and D are both equal to

1. There is no voltage drop across Z if no current is flowing as is the case for A, and all current at port 1 must equal the current port 2 since there is only one path for it to take, giving the result for D. This also gives a result of 0 for C, since an open at port 2 results in no current flow at port 1. Finally, B is the voltage over the current at port 1, which can be commonly recognized as the impedance. In this case, with port 2 shorted, that impedance is simply Z.

This process is carried out for several other simple building blocks which are featured in Table 4.1. These building blocks are used to create an ABCD parameter representation of a Mason equivalent circuit that is evaluated in MATLAB.

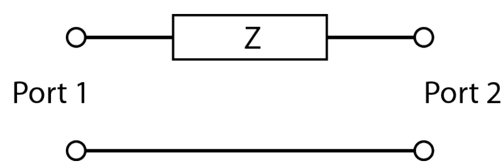

Figure 4.5: A simple series impedance used for the development of ABCD parameters for common circuit element blocks.

4.1.1.3 Mason Equivalent Circuit Parameters

The first layer created was the piezoelectric layer and was done by splitting the layer into simple blocks. Equation 4.5 represents the shunt and series capacitors and the transformer respectively connected to port 1.

$$\begin{bmatrix} 1 & 0 \\ -j\omega C_o & 1 \end{bmatrix} \begin{bmatrix} 1 & \frac{-1}{j\omega C_o} \\ 0 & 1 \end{bmatrix} \begin{bmatrix} \frac{1}{hC_o} & 0 \\ 0 & hC_o \end{bmatrix} \tag{4.5}$$

After the transformer, on the acoustic side, the three port piezoelectric layer must be made into a two port block for ABCD parameters to work. This is done by applying a fixed load to one port, representing the direction up, away from the substrate. In this case,

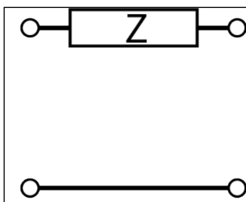	$\begin{bmatrix} 1 & Z \\ 0 & 1 \end{bmatrix}$
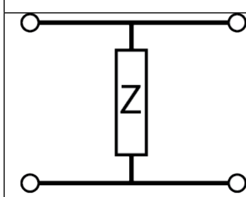	$\begin{bmatrix} 1 & 0 \\ \frac{1}{Z} & 1 \end{bmatrix}$
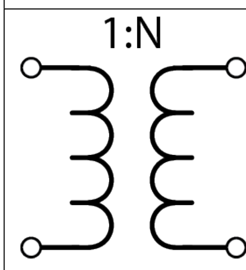	$\begin{bmatrix} \frac{1}{N} & 0 \\ 0 & N \end{bmatrix}$
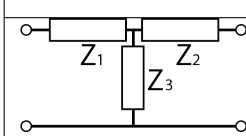	$\begin{bmatrix} 1+\frac{Z_1}{Z_3} & Z_1+Z_2+\frac{Z_1 Z_2}{Z_3} \\ \frac{1}{Z_3} & 1+\frac{Z_2}{Z_3} \end{bmatrix}$

Table 4.1: Table of ABCD parameter building blocks

the fixed load is an aluminum layer terminated in a short (Fig: 4.6), that when rearranged is now a two port network (Fig: 4.7).

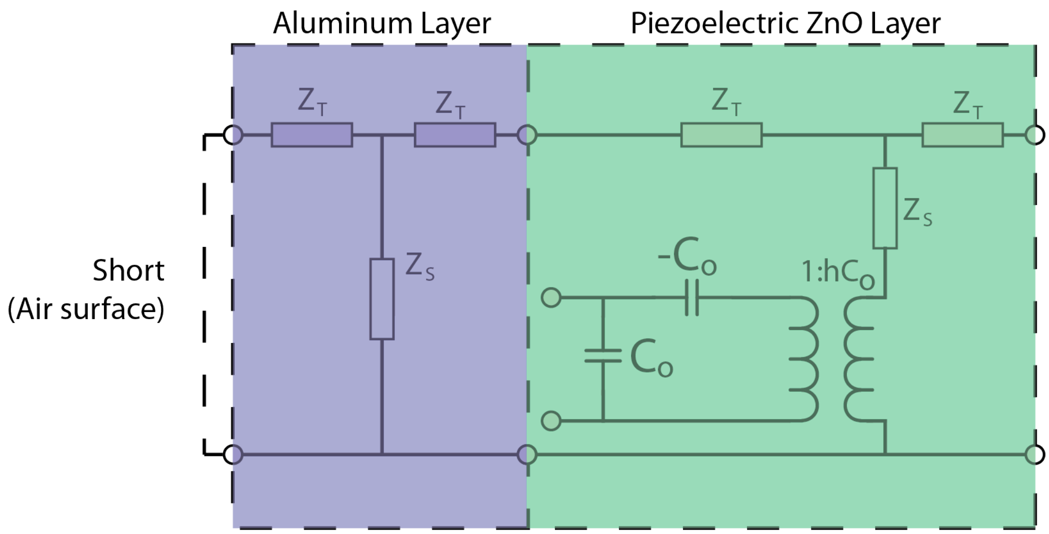

Figure 4.6: Mason equivalent circuit for a piezoelectric layer with aluminum top contact and short at the air interface.

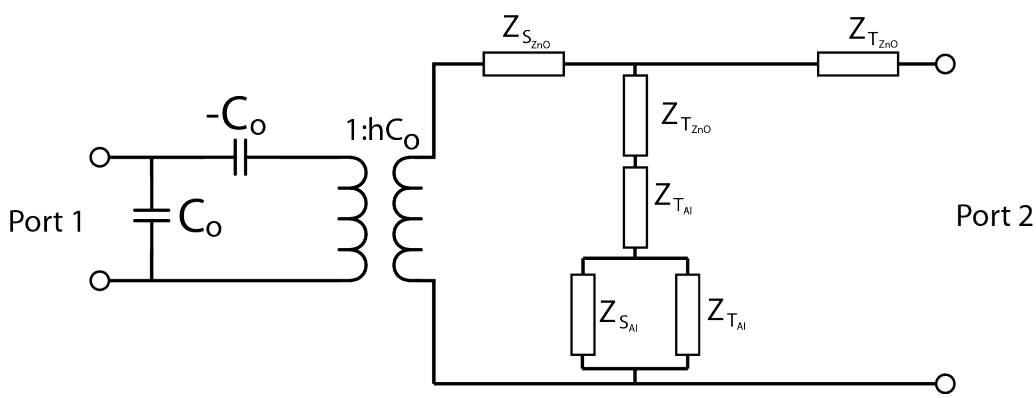

Figure 4.7: Mason equivalent circuit for a piezoelectric layer with aluminum top contact and short at the air interface rearranged to show two port nature.

$$\begin{bmatrix} 1 & Z_{S_{ZnO}} \\ 0 & 1 \end{bmatrix} \begin{bmatrix} 1 & 0 \\ \frac{1}{Z_{T_{ZnO}}+Z_{T_{Al}}+\frac{Z_{S_{Al}}Z_{T_{Al}}}{Z_{S_{Al}}+Z_{T_{Al}}}} & 1 \end{bmatrix} \begin{bmatrix} 1 & Z_{T_{ZnO}} \\ 0 & 1 \end{bmatrix} \tag{4.6}$$

The ABCD parameters for the network after the transformer, which includes the acoustic portion of the piezoelectric layer as well as the top aluminum layer is again broken down into simple blocks resulting in equation 4.6. With this portion established, underlying layers can be attached by creating ABCD parameters for the desired layer and multiplying through in series. For this work however, only a single layer was necessary, the bottom aluminum contact (Eq. 4.7).

$$\begin{bmatrix} 1+\frac{Z_{T_{Al}}}{Z_{S_{Al}}} & 2Z_{T_{Al}}+\frac{Z_{T_{Al}}^2}{Z_{S_{Al}}} \\ \frac{1}{Z_{S_{Al}}} & 1+\frac{Z_{T_{Al}}}{Z_{S_{Al}}} \end{bmatrix} \tag{4.7}$$

With all the building blocks in place, MATLAB is used to evaluate the resulting ABCD parameters describing the Mason equivalent circuit. In chapter 5 these simulation results will be discussed and compared with the measured results collected using the setup outlined in the following section.

4.1.2 S-Parameters

The measurement technique used to characterize and verify the operation of acoustic transducers uses a characterization technique called Scattering Parameters, or S-parameters for short. S-parameters are a tool used to characterize an RF ”black box” networks based on the signal applied and transmitted from the devices ports where the actual voltage and current may be difficult to measure practically. Fig. 4.8 and Eq. 4.8 define the interfaces to a two port network, with a being inputs and b outputs. S-parameters must also be defined with a characteristic impedance (Z_0). By definition, a port terminated in this impedance will absorb all of the signal, causing no signal to be reflected back. This means if port 2 is terminated in Z_0 a_2 will be zero by definition. Applying this to the expanded definition matrix (Eq. 4.9), a definition of each parameter can be determined (Eq. 4.10). When taking measurements, this characteristic impedance must be defined and calibrated accordingly in order to ensure accurate measurements. Practically, this means connecting the measurement tool to predefined loads, usually an open, short and through (open and short circuit and a matched connection between ports) for a two port measurement or open, short, load for 1 port.

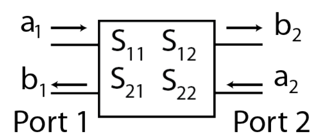

Figure 4.8: Interface definitions for an S-parameter network.

$$\begin{bmatrix} b_1 \\ b_2 \end{bmatrix} = \begin{bmatrix} S_{11} & S_{12} \\ S_{21} & S_{22} \end{bmatrix} \begin{bmatrix} a_1 \\ a_2 \end{bmatrix} \tag{4.8}$$

$$\begin{aligned} b_1 &= S_{11}a_1 + S_{12}a_2 \\ b_2 &= S_{21}a_1 + S_{22}a_2 \end{aligned} \tag{4.9}$$

$$\begin{aligned} S_{11} &= \frac{b_1}{a_1}\bigg|_{Z_2=Z_0} & S_{21} &= \frac{b_2}{a_1}\bigg|_{Z_2=Z_0} \\ S_{12} &= \frac{b_1}{a_2}\bigg|_{Z_1=Z_0} & S_{22} &= \frac{b_2}{a_2}\bigg|_{Z_1=Z_0} \end{aligned} \tag{4.10}$$

Unlike ABCD parameters, S-Parameters can be expanded for any number of ports by simply expanding the matrix, an N-port network can be represented by an $N \times N$ matrix of S-parameters. Unlike ABCD parameters however, S-parameters do not lend themselves to being connected in series. The fact that the output from a ABCD matrix operation is the input to the next network allows for cascading network by simply multiplying each network parameter matrix together. S-parameters on the other hand can not be cascaded so easily. To overcome this, another type of parameter, transfer parameters (T-parameters), are used that allow for easy cascading. T-parameters however are not used in this work and are simply mentioned for completeness. Details of the conversion between these different parameters can be found in [12].

4.1.3 Acoustic Transducer Measurement Setup

When characterizing the acoustic transducers, the reflection parameter, S_{11}, is used because it allows for the identification of a resonance in the device. With the help of the Mason Model simulation, the expected location of these resonances is known, but must be located. This location is visible in the S_{11} parameter as a dip in response. This dip is due to electrical energy being more effectively transformed into acoustic energy, with the resonant frequency being the optimal location. To find this, the measurement setup is very simple, the one port acoustic transducers are connected to Port 1 of the network analyzer. The challenge for this measurement comes from the difficulty in connecting to the device, which as seen in Fig. 3.10a, are small in size. This connection is accomplished using Cascade Microtech Infinity GSG-150 RF probes on a vibration isolated dual arm probe station. To allow for probing, contact pads are fabricated (Fig. 3.10a) with dimensions to match the probe spacing. As with all S-parameter measurements, calibration must be conducted to accurately report the device response. In this case, the probes must be included in the calibration. A calibration standard is used and consists of three structures, an open, short, and load. This allows the network analyzer to define the extremes of possible responses (Fig. 4.9) and map the measurements of the transducers in comparison. This calibration is done using a Cascade Microtrech-supplied calibration standard. For this calibration, the reference plane is located at the probe tips, as opposed to the end of the cables.

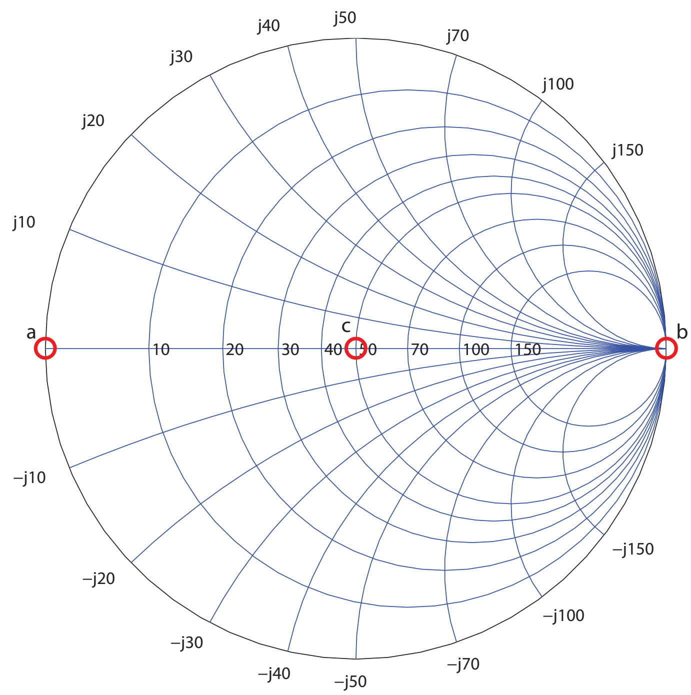

Figure 4.9: (a) Short, (b) open, and (c) 50 Ω load marked on a Smith chart. The network analyzer must be calibrated to best define these responses.

5. RESULTS

With a background in resonators, the fabrication techniques used to make acoustic transducers and the simulation model established, the outputs can be examined. In this chapter, the input parameters for the Mason Model simulation outlined in section 4.1.1 will be discussed and the outputs compared to measurements taken from devices made using the process outlined in section 3.3. Finally, additional physical effects are added to the simulation to improve the simulation agreement with the measured devices. These additions include effects such as series resistance and inductance, and acoustic attenuation within the transducer structure. The improved simulation results are again compared to the measured results and show a higher degree of agreement.

5.1 Results from Mason Model Simulation

Several tests are created to validate and characterize the simulation's operation and results. Plotted in these tests are the S_{11} parameters for the simulated device, with dips in response indicative of an effective transformation of electrical into acoustic energy. The data is displayed as magnitude plots, highlighting the frequency location and Q-factor of the acoustic resonances. For these tests, the Q-factor is calculated from a liner plot of the S_{11}-parameters taking the bandwidth to be the full-width-half-max. The test results featured in the following sections include: a single piezoelectric layer with varying thickness and "substrate," and a three layer device with varying electrode and ZnO thickness.

5.1.1 Single Piezoelectric Layer Simulation Results

The first tests are designed to highlight the piezoelectric layers electro-acoustic transduction properties and the effects of controllable external parameters, such as layer thickness and substrate termination.

5.1.1.1 Single Piezoelectric Layer with Varying Thickness

The thickness of the transducer layer has a major effect on the frequency operation since the fundamental resonance occurs when the acoustic wavelength is equal to twice the layer thickness, as discussed in section 2.1. Fig. 5.2 is a graph of the magnitude of the S_{11} and Z_{11} response from a single piezoelectric layer device as shown in Fig. 5.1.

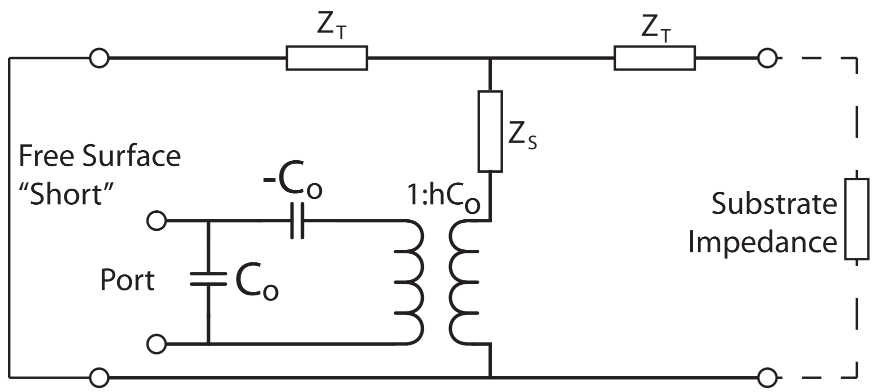

Figure 5.1: Lone piezoelectric layer simulated with various thicknesses and substrates.

As Fig. 5.2 shows, the resonant frequency follows the expected dependence to layer thickness based on the acoustic cavity described in section 2.1.1.1. When compared to the expected resonance frequency based on $1/2$ wavelength in ZnO with a velocity of $6135\frac{m}{s}$, there is complete agreement (Table 5.1). The changes in magnitude are a function of the impedance mismatch between the transducer and probe. As Fig. 5.2 shows, the closeer to the probe impedance of 50 Ω, the greater the transducer response. The input impedance at resonance is an important factor to consider when designing transducers as it has a large effect on the transducers electro-acoustic transduction efficiency.

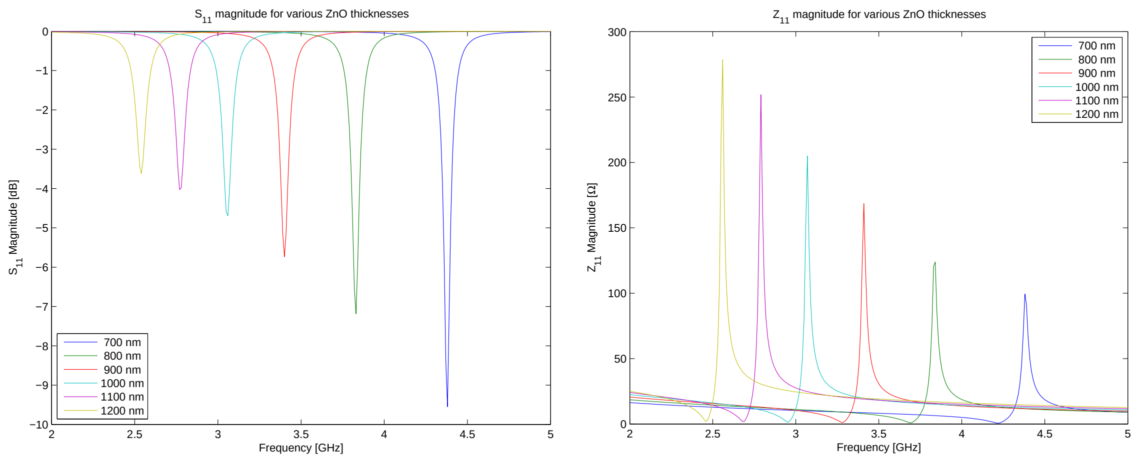

(a) (b)

Figure 5.2: (a) S_{11} and (b) impedance magnitude for a lone ZnO layer of various thicknesses terminated on both sides by air.

ZnO Thickness	Calculated Resonance	Simulated Resonance
700 nm	4.38 GHz	4.38 GHz
800 nm	3.83 GHz	3.83 GHz
900 nm	3.41 GHz	3.41 GHz
1000 nm	3.07 GHz	3.07 GHz
1100 nm	2.79 GHz	2.77 GHz
1200 nm	2.56 GHz	2.54 GHz

Table 5.1: Table of resonant frequencies for the lone ZnO layer from Fig. 5.2. Calculated resonance using Eq. 2.1

5.1.1.2 Single Piezoelectric Layer with Varying Termination

The second single layer simulation run is designed to test the effect of the substrate, or transducer mounting conditions. This can have a major impact on not only the Q-factor, but also on the mode of resonance. The simulated ZnO layer is mounted with two extreme conditions, free and fixed, and a realistic glass substrate, all taken to be infinatly thick, or thick enough that no reflections reach the surface again. The change from free to mounted on glass shows a reduction in Q-factor and a small change in resonant frequency ($\approx$ 10 MHz). However, when the surface is fixed, the resonant frequencies of the cavity are changed. For the free surface case, both sides of the cavity are effectively shorted, resulting in a resonance occurring when the particle velocity is at a maximum at both surfaces, as shown in Fig. 2.2, or for wavelengths of $\frac{vn}{2t}$ for all n $\{n = 1,2,3...\}$ with v the wave velocity. In the fixed case, the force is at a maximum at the mounted surface while velocity is maximized at the opposing free surface. This changes the boundary conditions for the cavity, causing the fundamental resonance to occur when the acoustic wavelength is four times the layer thickness, as opposed to the other case where it occurs at two times the thickness. Higher harmonics will continue to occur at $1/2$ wavelength intervals, or for wavelengths of $\frac{vn}{4t}$ for odd n $\{n = 1,3,5...\}$.

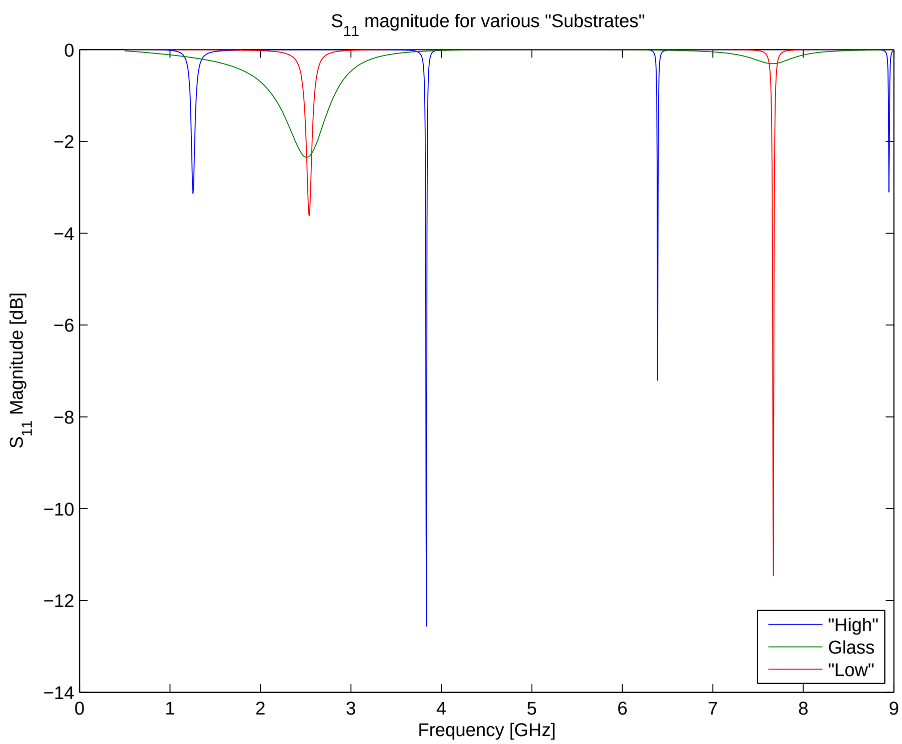

Figure 5.3: S_{11} magnitude for a 1.2 μm thick ZnO layer on various ”substrates.” A high impedance substrate is equivalent to a mounted and immobile surface and a low impedance represents a free surface.

Termination	Fundamental Resonance	2^{nd} Harmonic	3^{rd})
High (40Ω)	1.25 GHz	3.83 GHz	6.39 GHz
Glass (0.36Ω)	2.53 GHz	N/A	7.65 GHz
Low (0.05Ω)	2.54 GHz	N/A	7.67 GHz

Table 5.2: 1^{st}, 2^{nd} and 3^{rd} harmonic frequencies of 1.2 μm thick ZnO as a function of termination impedance from Fig. 5.3.

While the high impedance resonances occur at the expected 1/2 wavelength intervals, the low impedance termination and the glass substrate are only resonating at the odd harmonics. This is due to the conditions at the center of the cavity, where the model approximates the waves propagating from. Since velocity is modeled as away from the center, the center particles must have no velocity, placing another boundary condition on the possible resonances. This means that while displacement must be at a maximum at the surfaces, it must also be minimum at the center, limiting the resonance frequencies to the odd harmonics, as seen in Fig. 5.3.

5.1.2 Simulation Results with Electrode Layers

With the single piezoelectric layer simulations complete, electrode layers are added to the simulation (Fig. 5.4). These results should more accurately represent the acoustic response of the transducers as fabricated. Two variables are examined in this section, electrode thickness and piezoelectric layer thickness, both of which are mounted on a glass substrate.

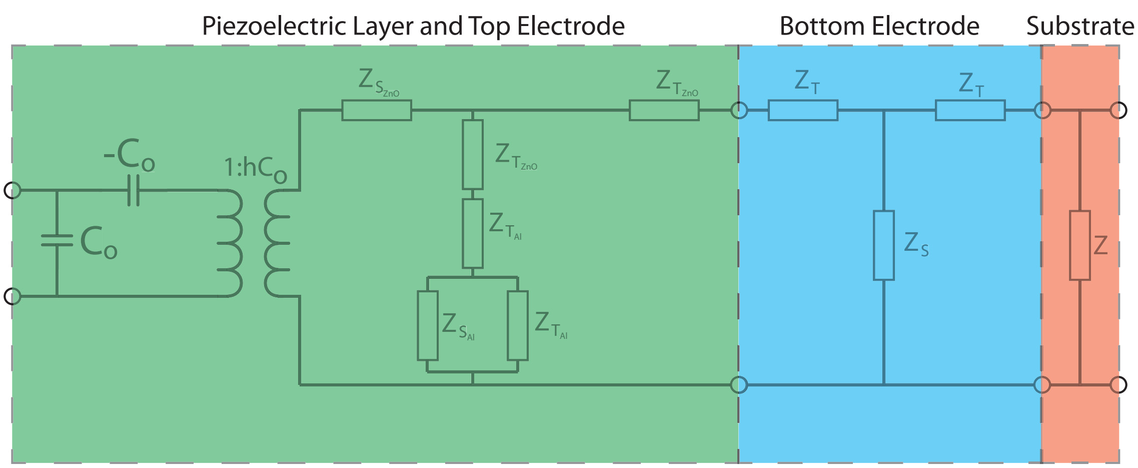

Figure 5.4: Three layer simulation stack. ZnO piezoelectric layer with two electrodes and mounted on a glass substrate.

5.1.2.1 Three Layer Stack with Varying Electrode Thicknesses

The first variable investigated is electrode thickness. With the addition of the electrode layers, the resonance cavity becomes more complicated. There are now more transitions in acoustic mediums, resulting in more reflections, complicating the resonance conditions. In Fig. 5.5, the electrode thickness is increased from a minimal 2 nm up to 400 nm, with a middle ground at 200 nm.

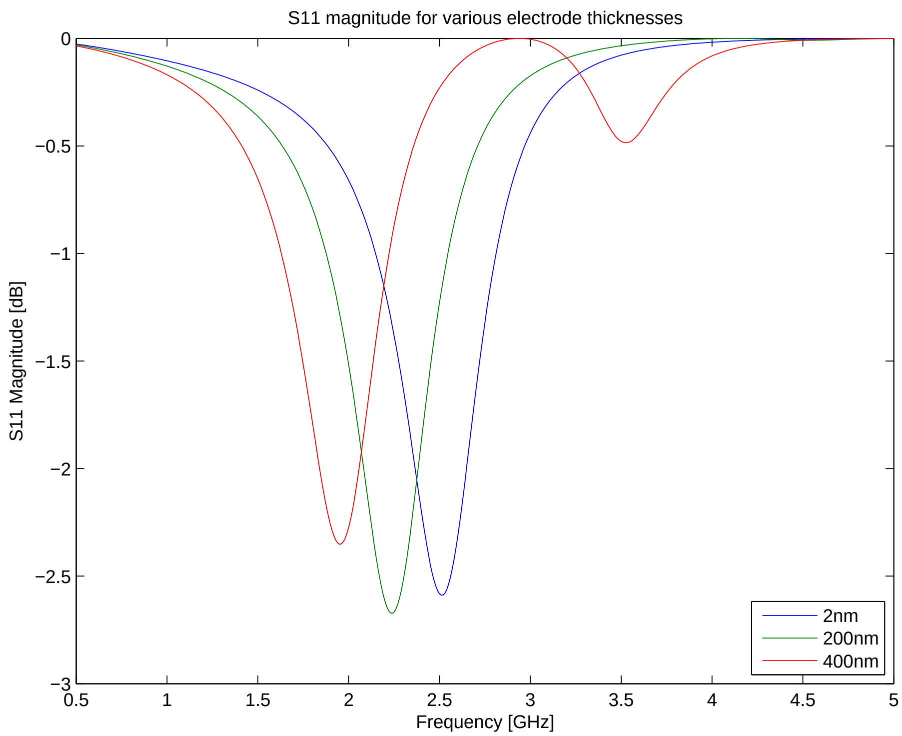

Figure 5.5: S_{11} magnitude for a 1.2 μm thick ZnO layer with various electrode thicknesses

Electrode Thickness	Resonance Frequency
2 nm	2.52 GHz
200 nm	2.24 GHz
400nm	1.95 GHz

Table 5.3: Resonance frequency of 1.2 μm thick ZnO as a function of Al electrode thickness from Fig. 5.5.

As the electrodes get thicker, the resonance is drawn away from the expected resonance of 2.56 GHz for a singular ZnO layer, as determined by the layer thickness. With increasing electrode thickness, the resonance frequency is reduced. This shift is due to the acoustic loading introduced by the metal layer and can have large effects for thin transducers such as the ones modeled here, where a 400 nm electrode changes the resonance frequency by over 20%. This shift is also in agreement with Rosenbaum [13], where a similar shift is observed when changing the electrode thickness on simulated devices.

Also observed is the appearance of a secondary resonance as the electrode thickness increases. This peak is from resonance modes within the electrode layers. These modes resonate in one or the other of the electrodes, offsetting them from the ZnO only modes, shifting the position of the center boundary condition. These modes are also explored more later in section 5.4.5.

5.1.2.2 Three Layer Stack with Varying Piezoelectric Thickness

The last verification simulation run is to confirm piezoelectric layer thickness dependence of the resonance frequency with the electrode layers present. In this simulation, the thickness of the electrodes is constant at 200 nm while the ZnO layer thickness is varied.

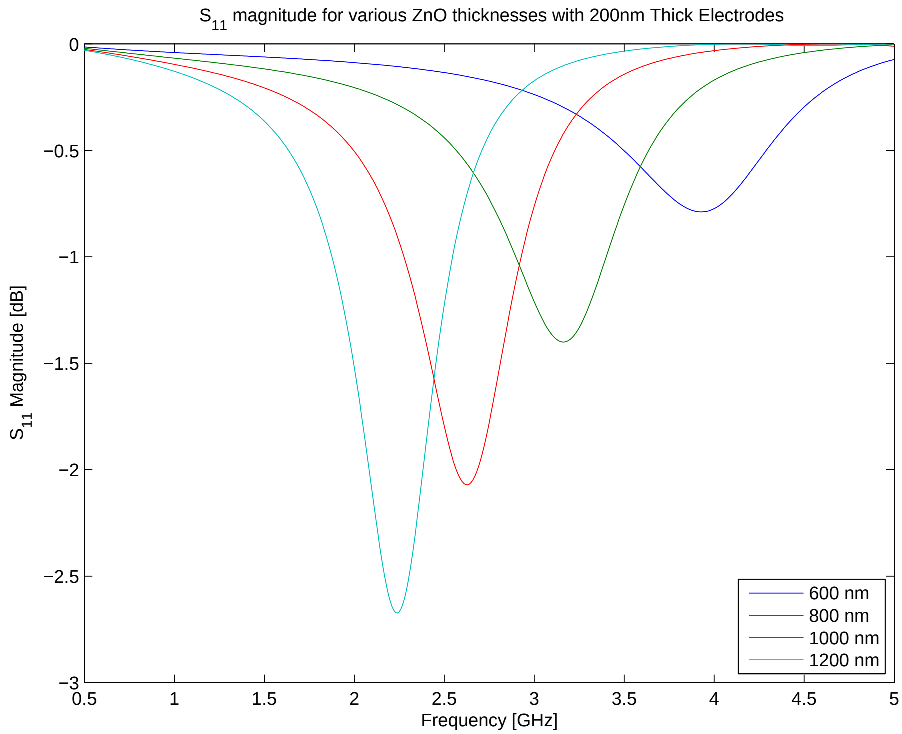

Figure 5.6: S_{11} magnitude for a transducer stack with 200 nm electrodes with various ZnO layer thicknesses

ZnO Thickness	Resonance Frequency
600 nm	3.95 GHz
800 nm	3.16 GHz
1000 nm	2.63 GHz
1200 nm	2.24 GHz

Table 5.4: Resonant frequency of 1.2 μm thick ZnO as a function of Al electrode thickness from Fig. 5.6.

Again, there is a clear, and expected, correlation between the ZnO layer thickness and the fundamental resonant frequency. We see resonance when the thickness equals

$1/2$ the acoustic wavelength with some apparent lengthening due to loading from the electrode layers. This effect is important to consider when designing transducers and matching networks.

We have now established a simulation that represents a three layer acoustic transducer that can be modeled with the same parameters as transducers fabricated in the clean room.

5.2 Fabricated Transducer Responses

Following the fabrication procedure discussed in section 3.3, acoustic transducers using a ZnO piezoelectric layer and Al electrodes were fabricated. In the following section, the measurement results of these transducers are presented and discussed. All transducers are fabricated on glass substrates with 200 nm thick electrodes, top and bottom, and varying piezoelectric thicknesses. From the transducers, S_{11} measurements are taken and plotted as impedances on Smith charts (Fig. 5.7) and magnitudes on a dB scale (Fig, 5.8).

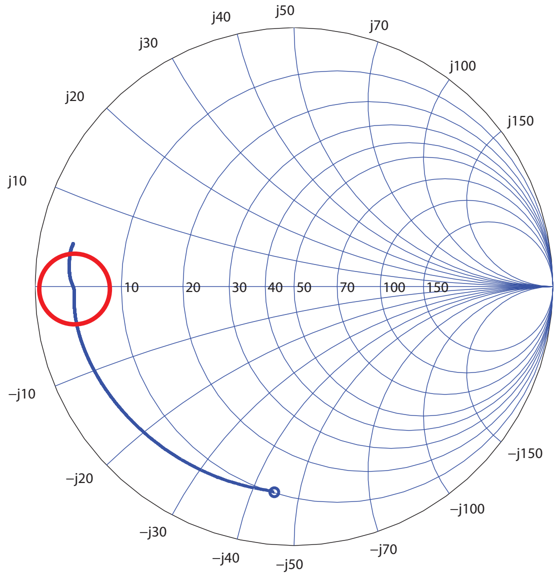

(a) 480 nm

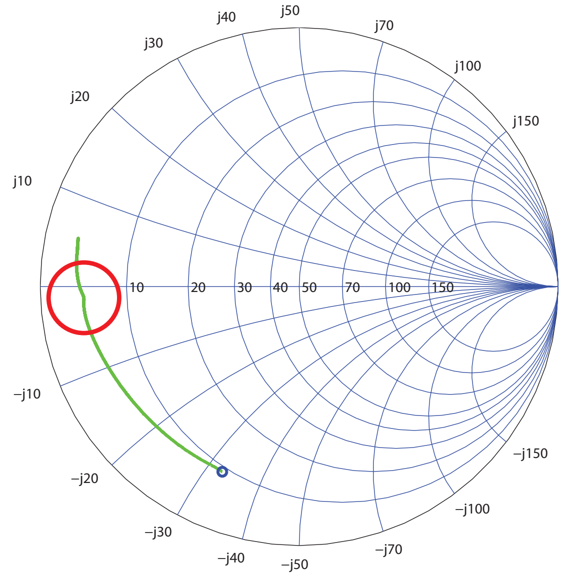

(b) 641 nm

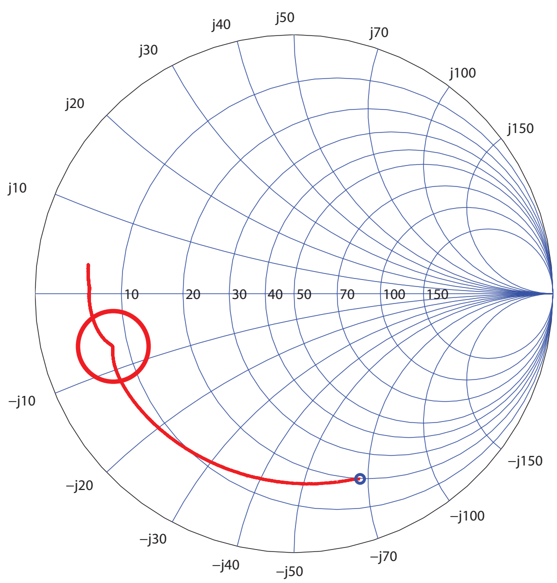

(c) 743 nm

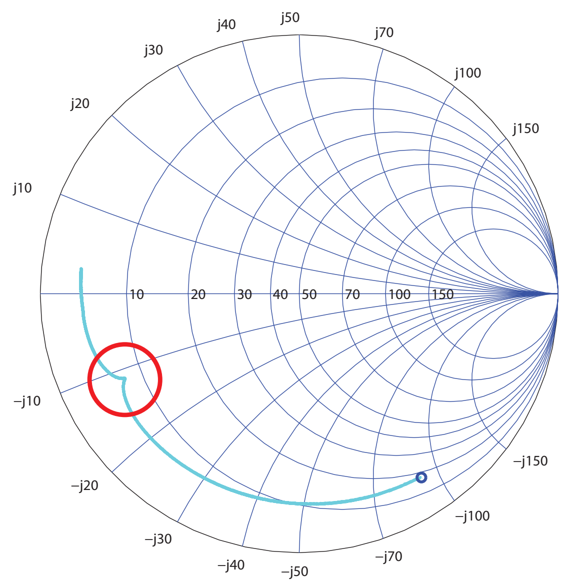

(d) 866 nm

Figure 5.7: Smith chart plots of measured S_{11} parameters for acoustic transducers with acoustic resonance highlighted. Measurements are from transducers with ZnO thicknesses of (a) 480 nm, (b) 641 nm, (c) 743 nm and (d) 866 nm with a frequency range of 0.4 GHz - 8 GHz for all devices.

When looking at the measurements from acoustic transducers plotted on Smith charts, resonance is located by looking for a different characteristic than on S_{11} magnitude plots. The drop in reflected power manifests as a move closed to the center of the plot, representing a matched load with no reflected power. This shows up on all four graphs as a dimple or bump in the otherwise smooth line, indicating the presence of a resonance. Plotting data on a Smith chart in this manner is extremely helpful when matching circuits, and in understanding the behavior of a circuit. What is not visible on the Smith chart however, is the frequency location of the resonances, which is best shown on S_{11} magnitude plots (Fig. 5.8).

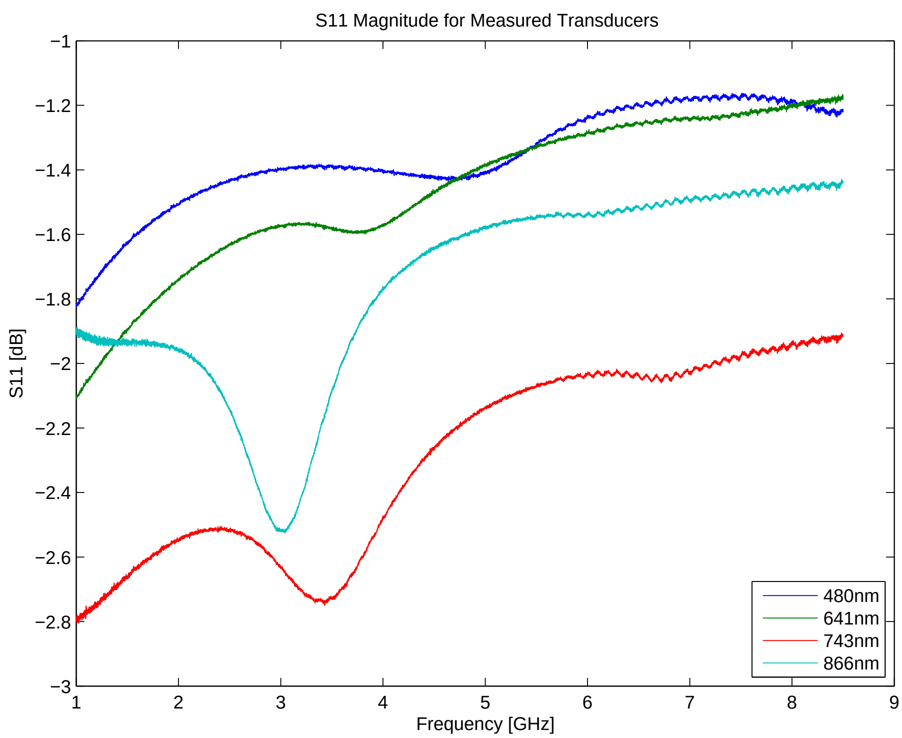

Figure 5.8: S_{11} magnitude measurement from four fabricated transducers with various ZnO thicknesses.

From the S_{11} plots (Fig. 5.8), a resonance is clearly visible for each transducer. The location for each device is presented in table 5.5. These measurements are compared to simulated results for devices with the same dimensions in the following section.

ZnO Thickness	Measured Resonance
480 nm	4.64 GHz
641 nm	3.82 GHz
743 nm	3.43 GHz
866 nm	3.04 GHz

Table 5.5: Measured resonant frequencies from Fig. 5.8 for fabricated acoustic transducers.

5.3 Comparison Between Simulated and Measured Responses

Now, the results measured from the fabricated transducers can compared to those of the simulated transducers. Simulations using the thicknesses of the fabricated devices, 200 nm thick electrodes with 866 nm (Fig. 5.9), 743 nm (Fig. 5.10), 641 nm (Fig. 5.11) and 480 nm (Fig. 5.12) thick ZnO layers is generated and compared to the measured results. The simulations results are plotted with their respective measured data on both magnitude and Smith chart plots for comparison.

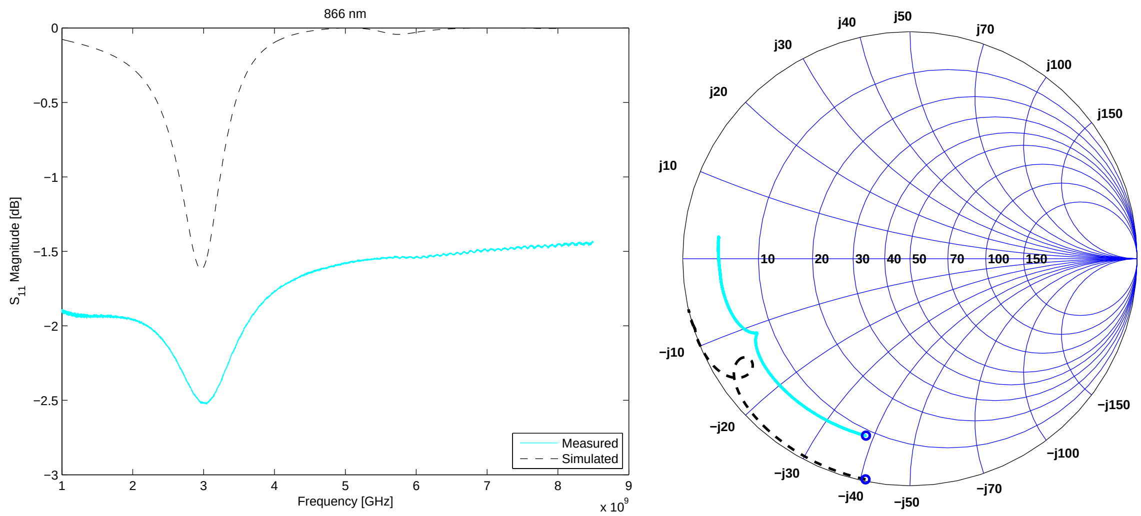

(a) (b)

Figure 5.9: Comparison between simulated and measured results for transducers having 866 nm thick ZnO layers. Comparisons are shown on a (a) magnitude plot and (b) Smith chart.

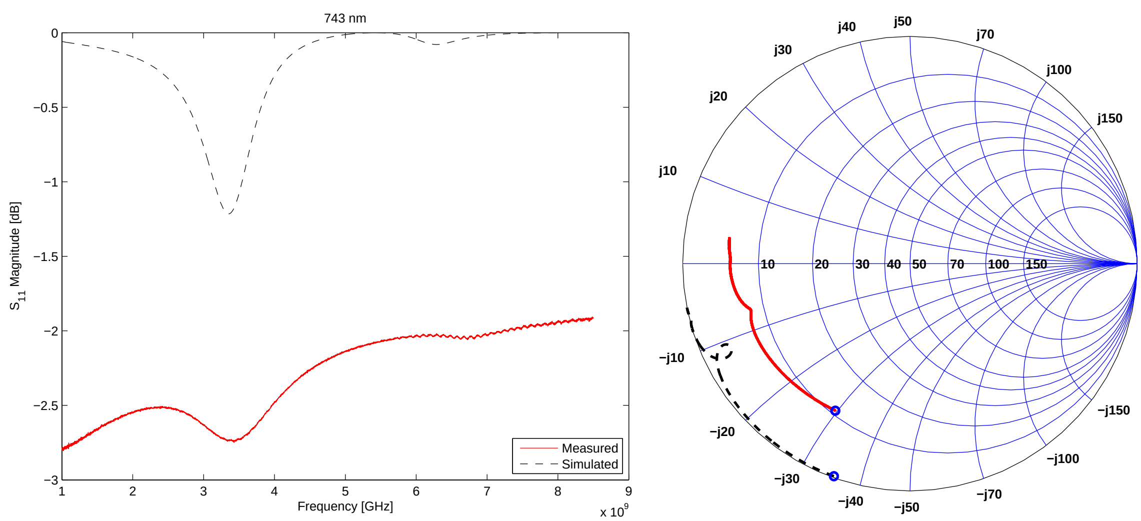

(a) (b)

Figure 5.10: Comparison between simulated and measured results for transducers having 743 nm thick ZnO layers. Comparisons are shown on a (a) magnitude plot and (b) Smith chart.

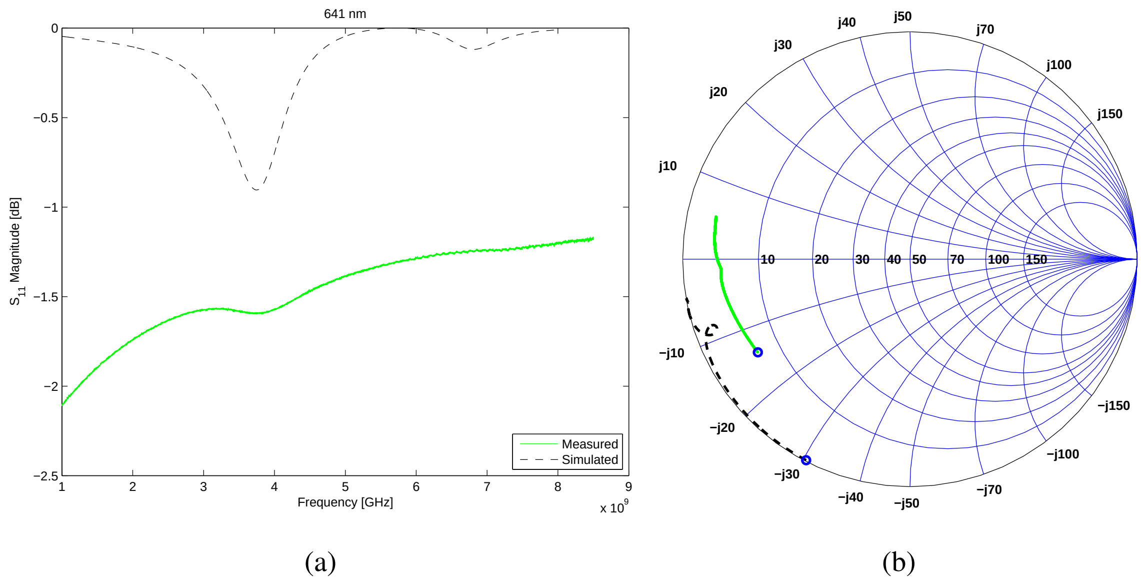

Figure 5.11: Comparison between simulated and measured results for transducers having 641 nm thick ZnO layers. Comparisons are shown on a (a) magnitude plot and (b) Smith chart.

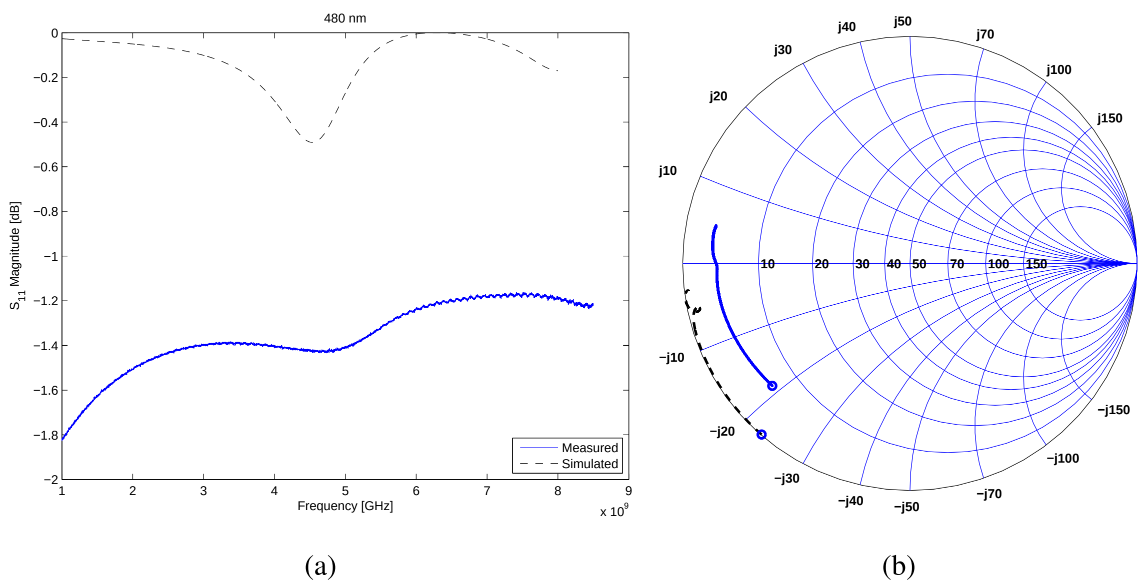

Figure 5.12: Comparison between simulated and measured results for transducers having 480 nm thick ZnO layers. Comparisons are shown on a (a) magnitude plot and (b) Smith chart.

ZnO Thickness	Simulated Resonance	Measured Resonance	% Difference
480 nm	4.54 GHz	4.64 GHz	2.15%
641 nm	3.75 GHz	3.82 GHz	1.83%
743 nm	3.36 GHz	3.43 GHz	1.16%
866 nm	2.98 GHz	3.04 GHz	1.97%

Table 5.6: A comparison of the measured and simulated resonances for fabricated acoustic transducers.

From a strictly resonance frequency location basis, the simulation and measurements show a very convincing level of agreement, with a difference of approximately 2% for all devices. This suggests that the simulation is modeling the operation of acoustic transducers, taking into account multiple layers and materials, as well as the effects of acoustic loading and substrate impedance mismatch. However, stark differences can be observed between the simulated and measured results. The measured results are offset on both the magnitude and Smith chart plots and the simulated results exhibit a much higher Q than the measured results. These differences make use of the the simulation results difficult for use in the design of matching networks for use with fabricated transducers. By identifying the causes of the differences, they can be added to the simulation, improving the simulation usefulness and expanding our understanding the the transducers operation.

5.4 Transducer Simulation Improvements

To account for the differences between the simulated and measured results, real world based additions can be included in the simulation that will greatly effect the response and improve the agreement between the two. These additions are made to both the electrical and acoustic side of the transducer equivalent circuit. They include effects such as series and shunt resistance, series inductance, and attenuation within the acoustic transducer, which was not included in the original simulation. Each of these additions are added to the simulation individually in the following sections in order identify their effects before being combined into a final improved simulation. All the simulations are run holding thickness parameters constant with an 800 nm thick ZnO layer and 200 nm thick Al electrodes all mounted on glass. S_{11} magnitudes are plotted on dB scale magnitude plots, and Z_{11} results are plotted on 50 Ω characteristic Smith charts.

5.4.1 Series Resistance

The first addition the the Mason model simulation is the inclusion of series resistance. Series resistance can come from many sources in the measurement setup used. The most likely sources in these experiments are from contact resistance between the probe tips and the aluminum pads and from resistance within the aluminum, especially at the connection over the step formed by the ZnO layer when connecting to the top electrode. The addition of series resistance reduces the reflected signal across all frequencies. This is seen on the magnitude plot (Fig. 5.14 a) as a frequency independent drop in the S_{11} response. On the Smith chart representation (Fig. 5.14 b), the plot moves closer to the center since less power is being reflected, looking like a better matched circuit.

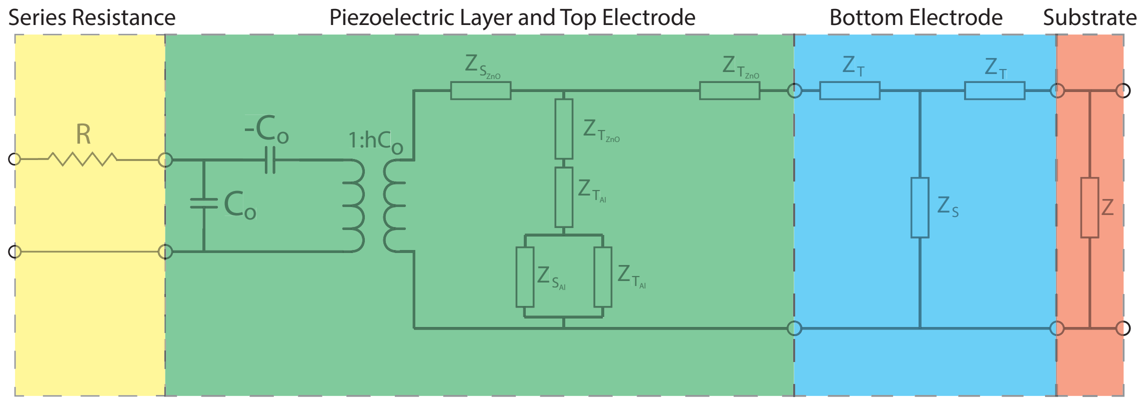

Figure 5.13: Equivalent circuit model with the addition of series resistance on the electrical port.

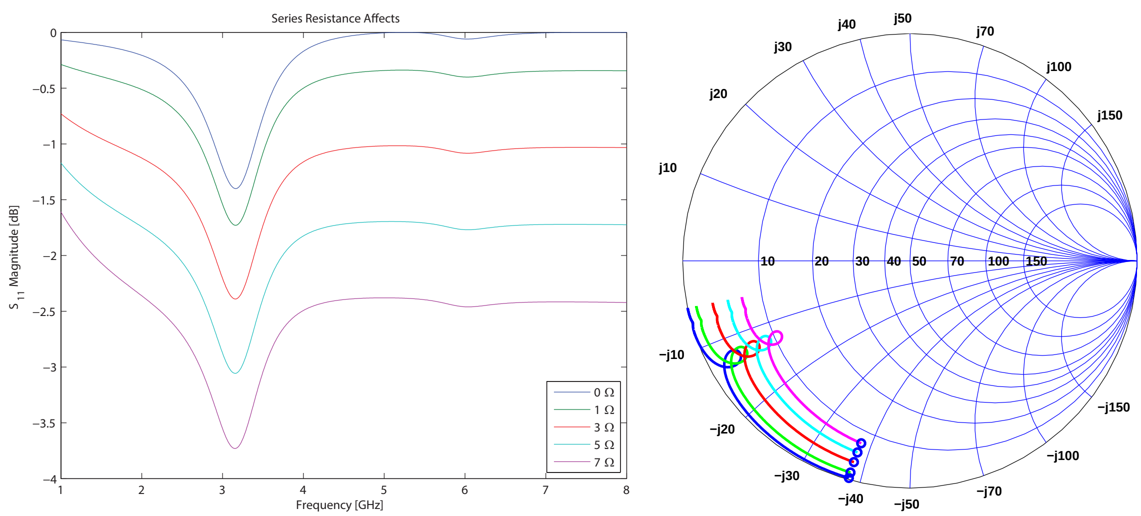

(a) (b)

Figure 5.14: Simulated S_{11} parameters with varying series resistance.

5.4.2 Shunt Resistance

The next effect modeled in the simulation is that of a shunt resistance. A shunt resistance results from unintended current flow between the device terminals. This can be because of imperfections in the pattern resulting in unintended connections or from current flow through the piezoelectric layer. At low frequencies, the capacitance of the transducer presents a large impedance causing current to flow through the shunt resistance. As the frequency increases, the impedance of the transducer reduces, drawing more current away from the shunt resistance, reducing it affect. This results in a frequency dependent shift in the reflected power. The magnitude plot (Fig. 5.16 a) shows a large drop in the S_{11} parameter for low frequencies, where the shunt resistance dominates the response. On the Smith chart, (Fig. 5.16 b) the drop in reflected power at low frequencies moves the response closer the the center, matched impedance point.

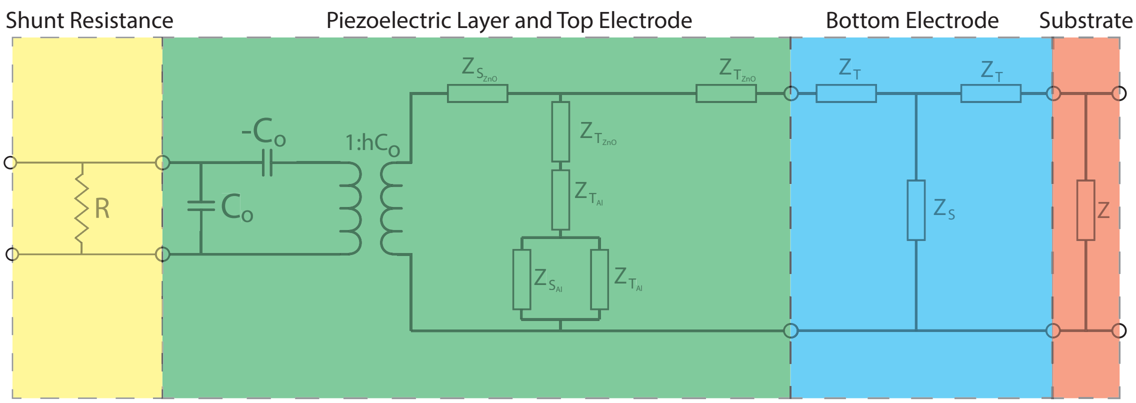

Figure 5.15: Equivalent circuit model with the addition of shunt resistance on the electrical port.

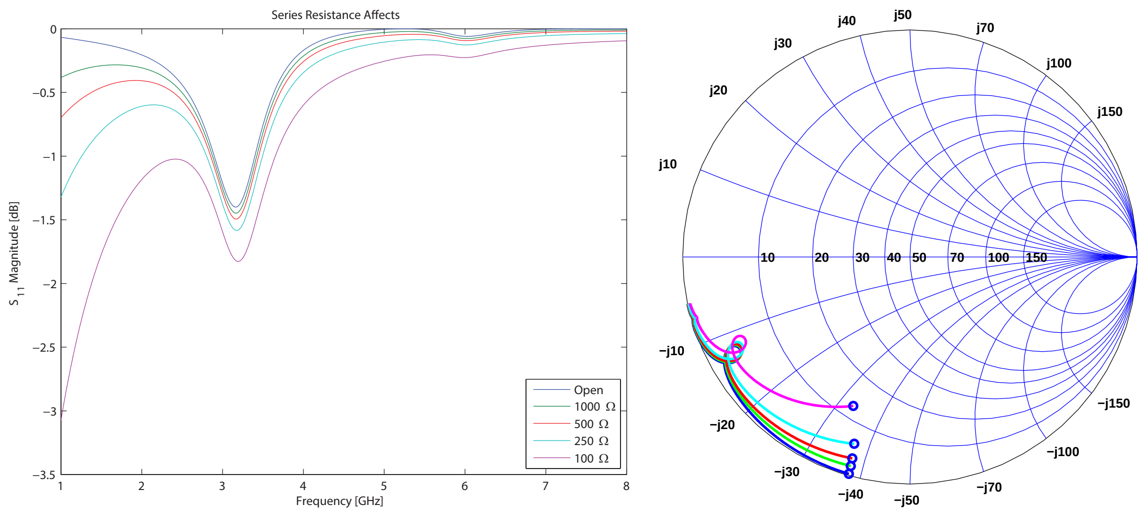

(a) (b)

Figure 5.16: Simulated S_{11} parameters with varying shunt resistance.

5.4.3 Series Inductance

Next, a series inductance is added to the simulation. This inductance comes from the leads connecting the probe touchdown pads to the transducer. The effect is especially important as the use of wire bonds in future transducer implementations will contribute a substantial inductance to the circuit that will need to be included in design considerations. The addition of a series inductance does not substantially alter the magnitude of the S_{11} response (Fig. 5.18 a), but does change the measured impedance of the transducer. The Smith chart (Fig. 5.18 b) shows a rotation toward the inductive half of the graph. This shift suggests that designed application of series inductance can be used to improve the impedance matching of the transducer.

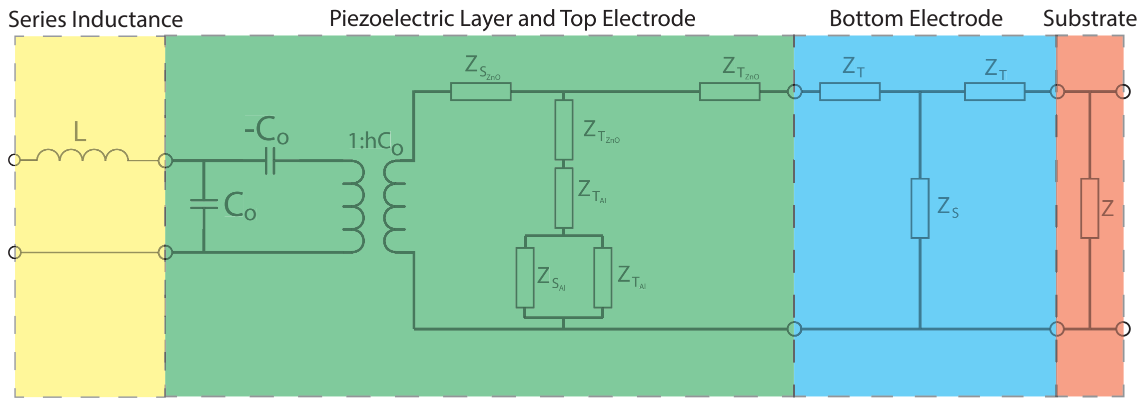

Figure 5.17: Equivalent circuit model with the addition of series inductance on the electrical port.

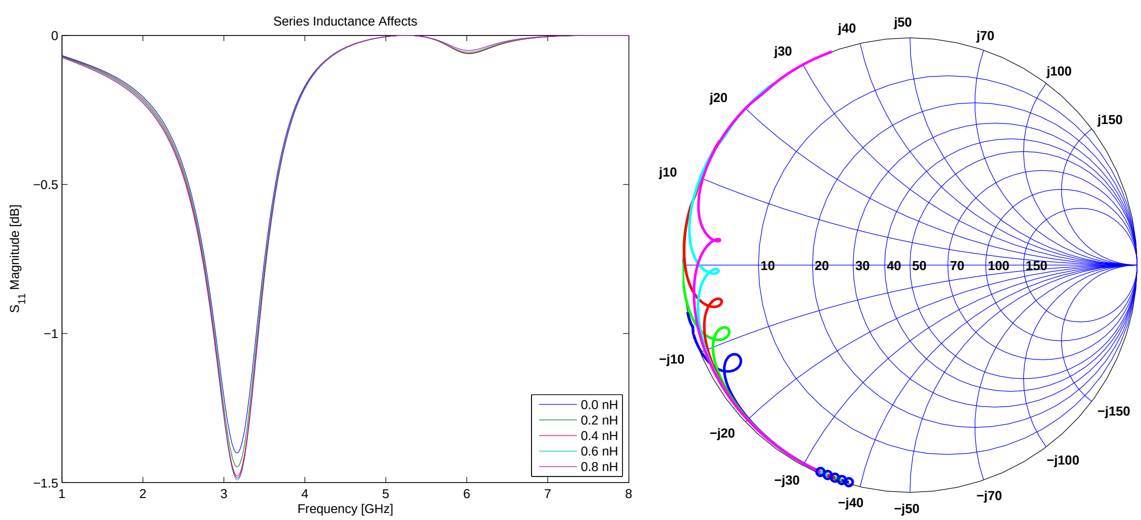

(a)

(b)

Figure 5.18: Simulated S_{11} parameters with varying series inductance

5.4.4 Acoustic Attenuation in Zinc Oxide

Now, modifications are made to the acoustic side of the simulation. The greatest drawback of the simulation initially implemented is the lack of attenuation within the acoustic layers. Attenuation can come from many sources, including, but not limited to, affects such as scattering and material viscosity. The attenuation added to this simulation groups all attenuation effects into a single frequency independent loss. These losses are modeled as a length dependent resistance added to the T-network representing the piezoelectric ZnO layer (Fig. 5.19). From the characteristic impedance equation in equ. 4.1, Z_0 has units of kg/s giving the new attenuation units of $kg(ms)^{-1}$. This attenuation is initially added to just the ZnO layer. The results are plotted in Fig. 5.20. Both graphs show a drop in transducer Q-factor as the attenuation is increased. This is expected, as more energy is lost during each oscillation. The magnitude plot also shows a slight shift in the resonant frequency, this also is expected, as the attenuation serves to effectively increase the load on the transducer.

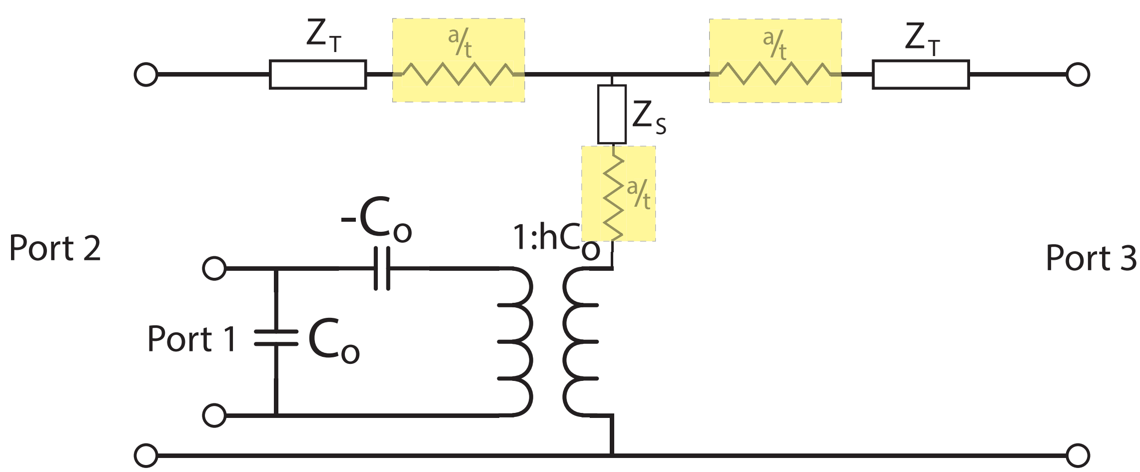

Figure 5.19: Mason equivalent circuit for a piezoelectric layer with the addition of attenuation.

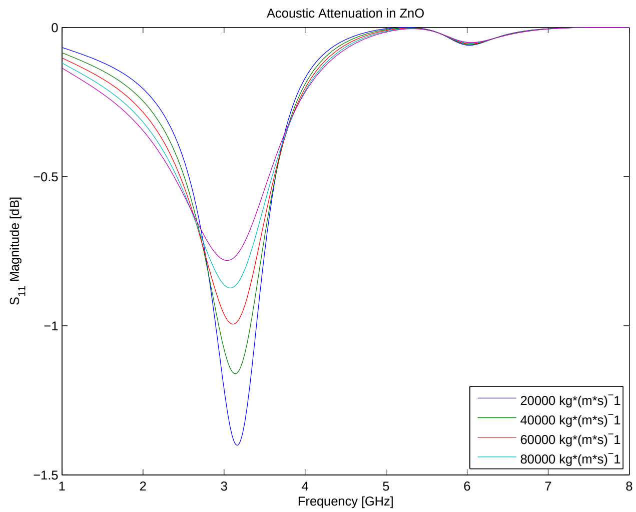

(a)

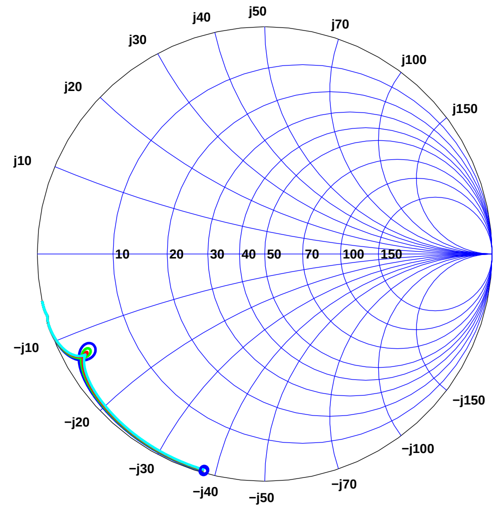

(b)

Figure 5.20: Simulated S_{11} parameters with varying ZnO acoustic attenuation.

5.4.5 Acoustic Attenuation in Aluminum

Finally, attenuation is added to the delay lines representing the Al electrodes. The same process as used for the piezoelectric layer is repeated for the inert layer T-networks (Fig. 5.21). The results, plotted in Fig. 5.22, show small changes in the resonator Q-factor and minimal change in the resonant frequency. This is expected, as the resonant properties of the transducer are dominated by the properties of the ZnO layer, which makes up most of the cavity. There is however, a greater effect on the secondary resonant peak caused by the presence of the transducers. This is because this resonance mode is located partially within the transducer layers, giving the properties of the Al a greater effect on the resonance.

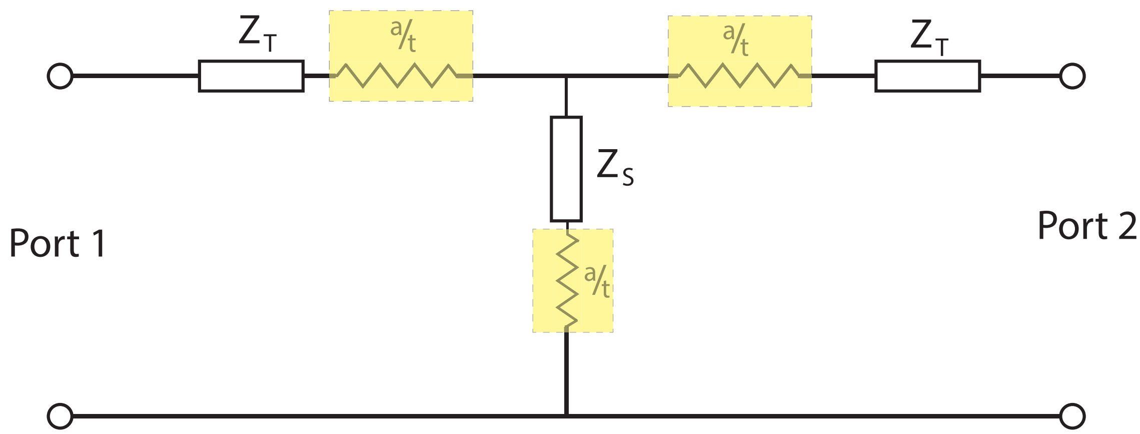

Figure 5.21: Mason equivalent circuit for an acoustic layer with the addition of attenuation.

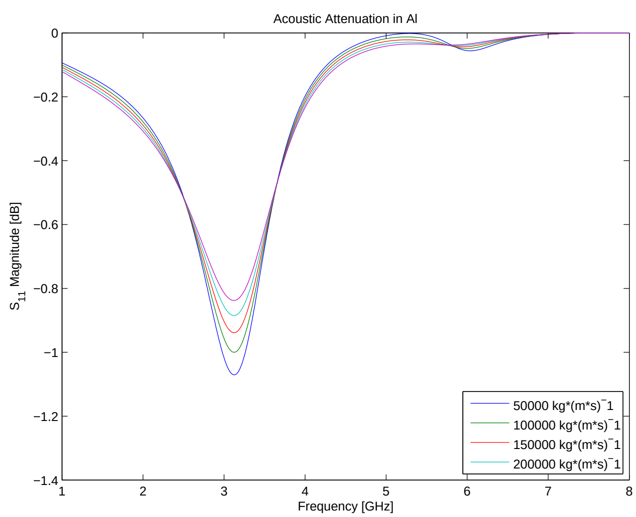

(a)

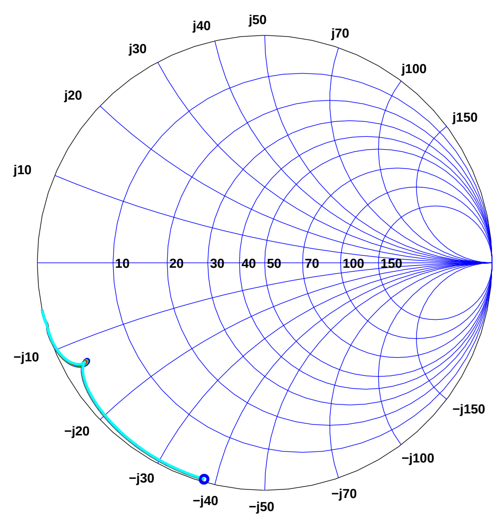

(b)

Figure 5.22: Simulated S_{11} parameters with varying Al acoustic attenuation.

5.5 Improved Simulation Comparison

With the new affects now included to the simulation, they can be fine tuned to better match the simulated and measured results. Electrical effects are tuned on an individual bases while attenuation effects are tuned to best match all cases. This is due to the fact that all the physical layer properties should be constant for all devices, while the electrical effects modeled can easily vary from device to device. These parameters are not necessarily the optimized or unique, but serve to demonstrate the presence of the affects in the fabricated devices and the improved usefulness of the simulation with their additions.

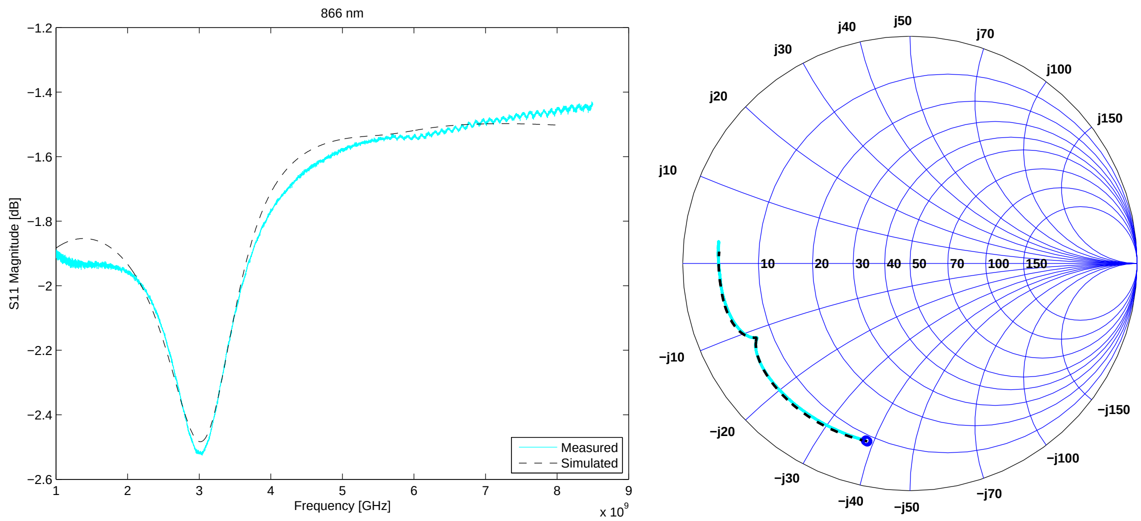

(a) (b)

Figure 5.23: Comparison between improved simulation and measured results for transducers having 866 nm thick ZnO layers. Comparisons are shown on a magnitude plot(a) and on a Smith chart (b).

Simulation Parameter	Value	Unit
Series Resistance	4.3	Ω
Shunt Resistance	400	Ω
Series Inductance	0.14	nH
ZnO Attenuation	11000	$\frac{kg}{ms}$
Al Attenuation	30000	$\frac{kg}{ms}$

Table 5.7: Parameters of the additional affects included in the simulation of 866 nm transducers.

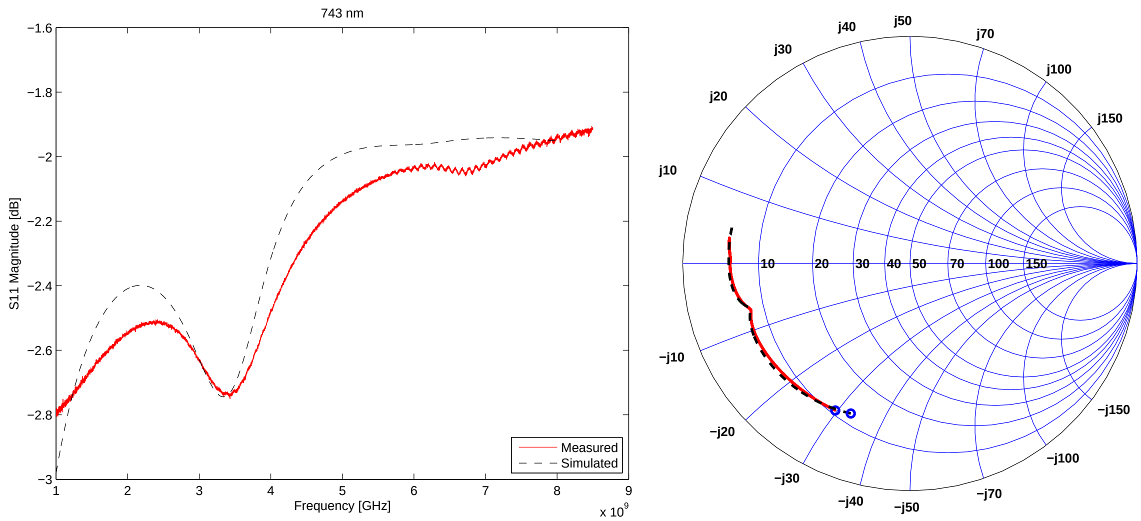

(a) (b)

Figure 5.24: Comparison between improved simulation and measured results for transducers having 743 nm thick ZnO layers. Comparisons are shown on a magnitude plot(a) and on a Smith chart (b).

Simulation Parameter	Value	Unit
Series Resistance	5.5	Ω
Shunt Resistance	175	Ω
Series Inductance	0.2	nH
ZnO Attenuation	11000	$\frac{kg}{ms}$
Al Attenuation	30000	$\frac{kg}{ms}$

Table 5.8: Parameters of the additional affects included in the simulation of 743 nm transducers.

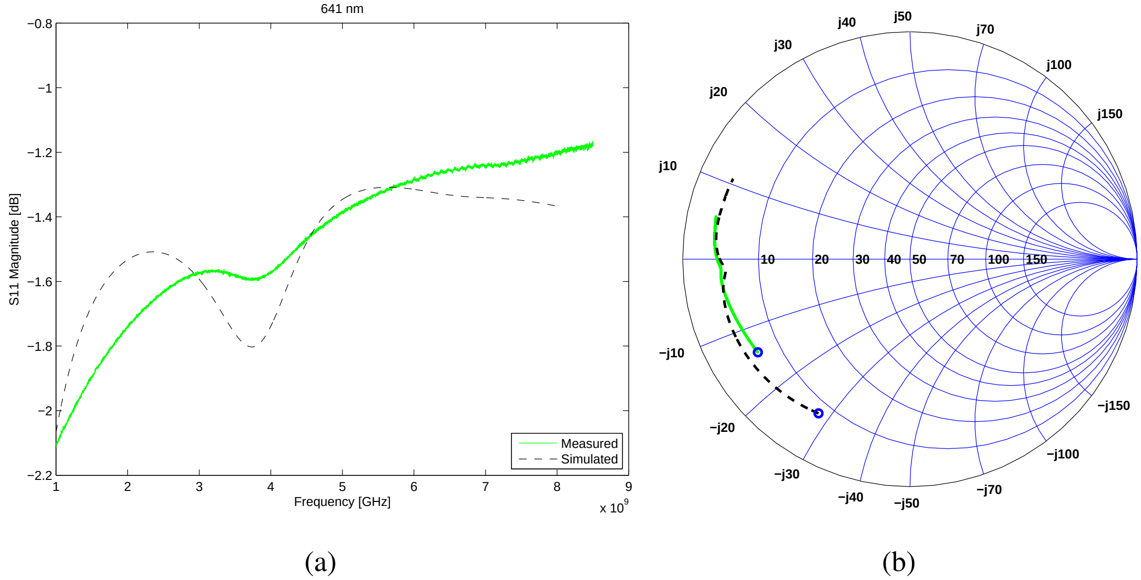

Figure 5.25: Comparison between improved simulation and measured results for transducers having 641 nm thick ZnO layers. Comparisons are shown on a magnitude plot(a) and on a Smith chart (b).

Simulation Parameter	Value	Unit
Series Resistance	3.5	Ω
Shunt Resistance	200	Ω
Series Inductance	0.3	nH
ZnO Attenuation	11000	$\frac{kg}{ms}$
Al Attenuation	30000	$\frac{kg}{ms}$

Table 5.9: Parameters of the additional affects included in the simulation of 641 nm transducers.

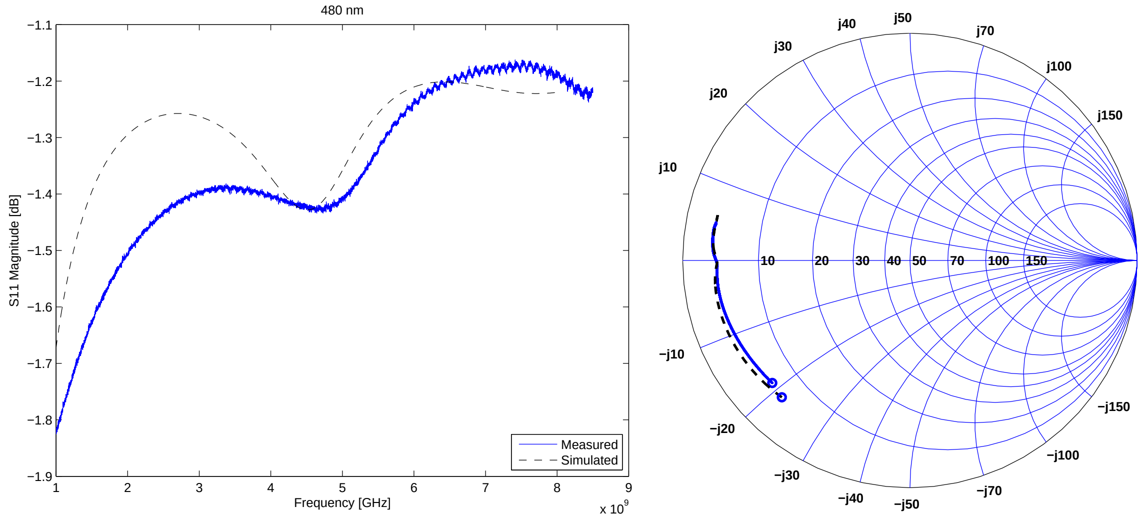

(a) (b)

Figure 5.26: Comparison between improved simulation and measured results for transducers having 480 nm thick ZnO layers. Comparisons are shown on a magnitude plot(a) and on a Smith chart (b).

Simulation Parameter	Value	Unit
Series Resistance	3.2	Ω
Shunt Resistance	200	Ω
Series Inductance	0.18	nH
ZnO Attenuation	11000	$\frac{kg}{ms}$
Al Attenuation	30000	$\frac{kg}{ms}$

Table 5.10: Parameters of the additional affects included in the simulation of 480 nm transducers.

When compared to the initial simulation results, the enhanced simulation shows a much greater degree of agreement with the measured results. The impedance parameters, as seen on the Smith charts, show a high level of agreement, making the simulations use in design of matching networks possible. Some devices still show some differences that appear clearly in some of the magnitude plots. These could be could be reduced further by continued tuning of simulation parameters or by the inclusion of more complex effects, such as frequency dependent attenuation and other higher order phenomenon.

6. CONCLUSION

The goal of the work presented here was to create a simulation of, and fabricate, thin-film bulk acoustic transducers for application in the parametric pumping of spin waves. A 1-D Mason-model-based representation of an acoustic transducer stack was created and several acoustic transducers were fabricated and measurements were taken. The conclusions drawn from this work, along with recommendations for the next steps in the project to create an acoustic spin wave pump, are presented here.

6.1 Summary

A base Mason model simulation was created using ABCD-parameters in MATLAB was created to model the operation of thin-film acoustic transducers. The model has been tested and characterized using several experiments, such as simulating a lone piezoelectric layer and a three layer transducer stack. The results obtained exhibit the characteristics expected from the transducer being modeled. However when compared to the results of fabricated transducers, the transducer impedance did not completely agree. Several additional phenomenon were identified as possible contributing factors the the disagreement between the simulated and measured results. These additions, series resistance, shunt resistance, series inductance, and acoustic attenuation, when added to the base model, greatly improved the agreement between the simulated and measured results. By optimizing these parameters to match measured results, the simulation can also be used to learn more about fabricated devices, such as attenuation or external electrical effects, rather then simply predicting device operation prior to fabrication. The equivalent circuit model presented is deemed an accurate model of acoustic transducer response and is a valuable tool for the design of transducer circuit design. Improvements can still be made to the simulation, such as a better representation of the acoustic attenuation mechanisms. [14] offers a method of representing material properties as complex coefficients which might improve the results obtained from the simulation.

The fabrication process is also deemed a success. Several devices have been fabricated with varying thicknesses resulting in resonant responses that fall close to a first order approximation frequency, with the difference accounted for in the simulation by the presence of acoustic loading caused by the presence of electrodes. This process is ready for application in the next stages of the acoustic spin wave pump project.

6.2 Future Work

The next step of the project is to integrate the acoustic transducer with a spin wave excitation/measurement setup (Fig. 6.1). For this stage, acoustic transducers are patterned onto GGG (Gadolinium Gallium Garnet) substrates with a magnetic Yttrium Iron Garnet (YIG) thin film on the opposing face. GGG has low acoustic losses and functions as a cavity forming a High-Overtone Bulk Acoustic Resonator. This resonator will be used to apply stress and strain the YIG thin film, altering its magnetic properties. These properties effect the oscillation and propagation of spin waves, and when varied at twice the spin wave frequency will parametrically pump the propagating spin wave.

This integration process may pose challenges as the spin wave is propagated in a YIG waveguide whose shape, a thin strip approximately 2-3 mm wide, makes measurement and connections difficult. A spin wave excitation/measurement setup has been created but was not presented in this work. At this point, the best connection method available is a wire bond from a stripline patterned on a PCB, allowing for a connection to the acoustic transducer. This will most likely require the design of a matching net-

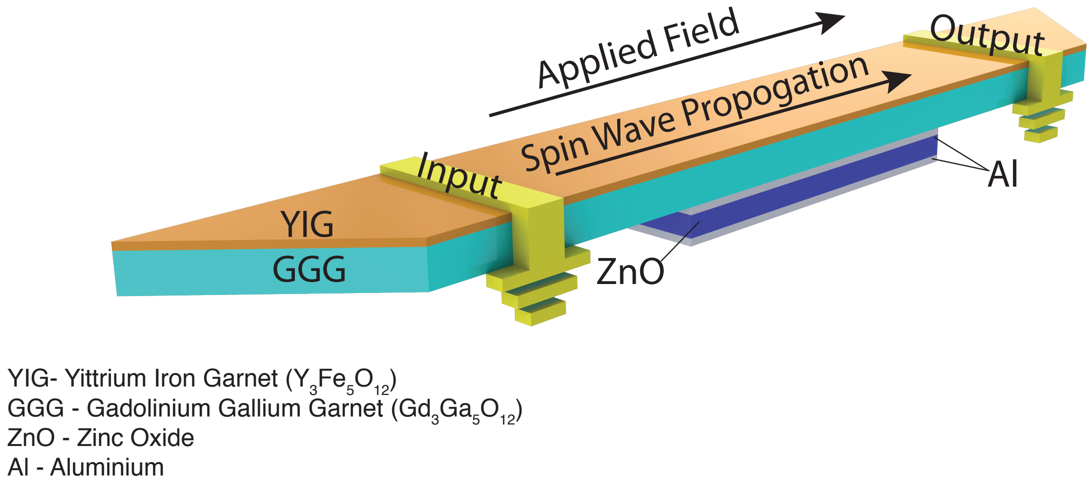

Figure 6.1: Diagram showing an integrated acoustic spin wave pump. The transducer presented in this work is patterned onto the YIG spin wave waveguide.

work to maximize the RF power transfered to the transducer and into acoustic waves. The transducer itself can most likely be pattered directly onto the YIG substrate using a shadow mask to pattern the layers since the probe landing pads required for the test devices described here will not be needed.

BIBLIOGRAPHY

1. M. Kostylev, A. Serga, T. Schneider, B. Leven, and B. Hillebrands, “Spin-wave logical gates,” *Applied Physics Letters*, vol. 87, no. 15, pp. 153 501 – 153 501–3, 2005.

2. T. Schneider, A. Serga, B. Leven, B. Hillebrands, R. Stamps, and M. Kostylev, “Realization of spin-wave logic gates,” *Applied Physics Letters*, vol. 92, no. 2, pp. 022 505–022 505–3, 2008.

3. W. P. Mason, *Electromechanical transducers and wave filters*. Princeton, NJ: Van Nostranc Co., 1948.

4. W. Mason, *Physical Acoustics and The Properties of Solids*. Princeton, NJ: Van Nostranc Co., 1958.

5. G. Guilbault, B. Hock, and R. Schmid, “A piezoelectric immunobiosensor for atrazine in drinking water,” *Biosensors and Bioelectronics*, vol. 7, no. 6, pp. 411–419, 1992.

6. J. G. Drenthen and G. de Boer, “The manufacturing of ultrasonic gas flow meters,” *Flow Measurement and Instrumentation*, vol. 12, no. 2, pp. 89 – 99, 2001.

7. J. G. Gualtieri, J. A. Kosinski, and A. Ballato, “Piezoelectric materials for acoustic wave applications,” *IEEE Transactions on Ultrasonics, Ferroelectrics, and Frequency Control*, vol. 41, no. 1, pp. 53–59, 1994.

8. P. Gopal and N. A. Spaldin, “Polarization, piezoelectric constants, and elastic constants of zno, mgo, and cdo,” *Journal of Electronic Material*, vol. 35, no. 4, 2006.

9. S. Wolf and R. Tauber, *Silicon Processing for the VLSI Era, Vol 1: Process Technology*. Sunset Beach CA: Lattice Press, 2000.

10. R. Krimholtz, D. Leedom, and G. Matthaei, “New equivalent circuits for elementary piezoelectric transducers,” *Electronics Letters*, vol. 6, no. 12, pp. 398 – 399, 1970.

11. S. Sherrit, S. Leary, B. Dolgin, and Y. Bar-Cohen, “Comparison of the mason and klm equivalent circuits for piezoelectric resonators in the thickness mode,” in *Ultrasonics Symposium, 1999. Proceedings. 1999 IEEE*, vol. 2, 1999, pp. 921 – 926.

12. D. A. Frickey, “Conversions between S, Z, Y, h, ABCD, and t parameters which are valid for complex source and load impedances,” *IEEE Transactions on Microwave Theory and Techniques*, vol. 42, no. 2, pp. 205–211, 1994.

13. J. Rosenbaum, *Bilk Acoustic Wave Theory and Devices*. 685 Canton Street Norwood, MA 02062: Artech House, 1988.

14. R. Holland, “Representation of dielectric, elastic, and piezoelectric losses by complex coefficients,” *IEEE Transactions on Sonics and Ultrasonics*, vol. SU-14, no. 1, pp. 18–20, 1967.

APPENDICES

A. MASON MODEL MATLAB CODE

Table of Contents

Define Function

```
function [ S11, Z11 ] = Mason_Model( t_ZnO, f_start, f_step, f_stop ,
    Zo_sub, t_Al_top, t_Al_bot, Series, L, ZnO_Loss, Al_Loss, Shunt_R )
% Mason Model
%   t_ZnO   : ZnO layer thickness [m]
%   f_start : Frequency sweep start [Hz]
%   f_step  : Frequency sweep step [Hz]
%   f_stop  : Frequency sweep stop [Hz]
%   Zo_sub  : Substrate impedance [Kg/s]
%   t_Al_top: Top electrode thickness [m]
%   t_Al_bot: Bottom electrode thickness [m]
%   Series  : Series resistance [ohm]
%   L       : Series Inductance [H]
%   ZnO_Loss: ZnO layer attenuation [Kg m/s]
%   Al_Loss : Electrode layer attenuation [Kg m/s]
%   Shunt_R : Shunt resistance [ohm]
```

Define Global Constants

```
Area = pi*(100e-6)^2; %device area  [m^2]
f = f_start:f_step:f_stop;
syms('w');
```

ZnO Layer Constants

```
den_ZnO = 5606; %density    [kg/m^3]
perm_ZnO = 10.9*8.854e-12; %Permitivity [F/m]
e33_ZnO = 1.34; %Piezoelectric constant [C/m^2]
c33_ZnO = 2.11*10^11; %Elastic stiffness constant [N/m^2]
v_ZnO = sqrt(c33_ZnO/den_ZnO); %acoustic velocity [m/s]

Zo_ZnO = v_ZnO*den_ZnO*Area;
k_ZnO = w/v_ZnO;
```

Al Layer Constants

```
den_Al = 2700; %Density of Al [Kg/m^3]
v_Al = 5000; %Acoustic Velocity in Al [m/s]

Zo_Al = den_Al*v_Al*Area;
k_Al = w/v_Al;
```

Substrate Material Constants

```
v_glass = 3962; %Acoustic Velocity in Al [m/s]
den_glass = 2648; %Density of Glass [Kg/m^3]
```

Transformer Matrix

```
Co = perm_ZnO*Area/t_ZnO;
Kt = sqrt(e33_ZnO^2/(c33_ZnO*perm_ZnO));
h = Kt*sqrt(c33_ZnO/perm_ZnO);

Matrix_1 = [1,Series;0,1]*[1,0;1/Shunt_R,1]*[1,1i*w*L;0,1]*
    [1,0;1i*w*Co,1]*[1,-1/(1i*w*Co);0,1]*[1/(h*Co),0;0,(h*Co)];
```

ZnO with top Al Electrode Matrix

```
Zs_ZnO = -1i*Zo_ZnO/sin(k_ZnO*t_ZnO)+ZnO_Loss*t_ZnO;
Zt_ZnO =  1i*Zo_ZnO*tan(k_ZnO*t_ZnO/2)+ZnO_Loss*t_ZnO;

Zs_Al_top = -1i*Zo_Al/sin(k_Al*t_Al_top)+Al_Loss*t_Al_top;
Zt_Al_top =  1i*Zo_Al*tan(k_Al*t_Al_top/2)+Al_Loss*t_Al_top;

Matrix_2 = [1,Zs_ZnO;0,1]*[1,0;1/(Zt_ZnO+Zt_Al_top+(Zs_Al_top*Zt_Al_top)/
    (Zs_Al_top+Zt_Al_top)),1]*[1,Zt_ZnO;0,1];
```

Al Layer Matrix

```
Zs_Al_bot = -1i*Zo_Al/sin(k_Al*t_Al_bot)+Al_Loss*t_Al_bot;
Zt_Al_bot =  1i*Zo_Al*tan(k_Al*t_Al_bot/2)+Al_Loss*t_Al_bot;

Matrix_Al = [1+Zt_Al_bot/Zs_Al_bot,2*Zt_Al_bot+Zt_Al_bot^2/Zs_Al_bot;1/
    Zs_Al_bot,1+Zt_Al_bot/Zs_Al_bot];
```

Substrate Matrix

```
Matrix_sub = [1,0;1/Zo_sub,1];
```

Final Matrix

```
Matrix_Total=Matrix_1*Matrix_2*Matrix_Al*Matrix_sub;
```

Evaluate Matrix

```
Zo = 50;
A_M = Matrix_Total(1,1);
B_M = -Matrix_Total(1,2);
C_M = Matrix_Total(2,1);
D_M = -Matrix_Total(2,2);

size = length(f);

A = zeros(size,1);
B = zeros(size,1);
C = zeros(size,1);
D = zeros(size,1);

parfor x = 1:size
        A(x,1)=subs(A_M,'w',f(:,x)*2*pi);
        B(x,1)=subs(B_M,'w',f(:,x)*2*pi);
        C(x,1)=subs(C_M,'w',f(:,x)*2*pi);
        D(x,1)=subs(D_M,'w',f(:,x)*2*pi);

end

S11 = (A.*Zo+B-C.*Zo.*Zo-D.*Zo)./(A.*Zo+B+C.*Zo.*Zo+D.*Zo);
Z11 = A./C;
```

Published with MATLAB® 7.14